Comput. Methods Appl. Mech. Engrg. 197 (2008) 4333–4352

Contents lists available at ScienceDirect

Comput. Methods Appl. Mech. Engrg.

journal homepage: www.elsevier.com/locate/cma

Isogeometric analysis of the Cahn–Hilliard phase-field model

Héctor Gómez [a,b,*], Victor M. Calo [a], Yuri Bazilevs [a], Thomas J.R. Hughes [a]

[a] Institute for Computational Engineering and Sciences, The University of Texas at Austin, 1 University Station, C0200, 201 E. 24th Street, Austin, TX 78712, United States
[b] Group of Numerical Methods in Engineering, Department of Mathematical Methods, University of A Coruña, Campus de Elviña, 15192 A Coruña, Spain

ARTICLE INFO

Article history:
Received 11 December 2007
Received in revised form 23 April 2008
Accepted 6 May 2008
Available online 13 May 2008

Keywords:
Phase-field
Cahn–Hilliard
Isogeometric analysis
NURBS
Steady state solutions
Isoperimetric problem

ABSTRACT

The Cahn–Hilliard equation involves fourth-order spatial derivatives. Finite element solutions are not common because primal variational formulations of fourth-order operators are only well defined and integrable if the finite element basis functions are piecewise smooth and globally $\mathscr{C}^1$-continuous. There are a very limited number of two-dimensional finite elements possessing $\mathscr{C}^1$-continuity applicable to complex geometries, but none in three-dimensions. We propose isogeometric analysis as a technology that possesses a unique combination of attributes for complex problems involving higher-order differential operators, namely, higher-order accuracy, robustness, two- and three-dimensional geometric flexibility, compact support, and, most importantly, the possibility of $\mathscr{C}^1$ and higher-order continuity. A NURBS-based variational formulation for the Cahn–Hilliard equation was tested on two- and three-dimensional problems. We present steady state solutions in two-dimensions and, for the first time, in three-dimensions. To achieve these results an adaptive time-stepping method is introduced. We also present a technique for desensitizing calculations to dependence on mesh refinement. This enables the calculation of topologically correct solutions on coarse meshes, opening the way to practical engineering applications of phase-field methodology.

1. Introduction

1.1. Phase transition phenomena: the phase-field approach

Two different approaches have been used to describe phase transition phenomena: *sharp-interface* models and *phase-field* (diffuse-interface) models. Traditionally, the evolution of interfaces, such as the liquid–solid interface, has been modeled using sharp-interface models [37,72]. This entails the resolution of a moving boundary problem. Thus, the partial differential equations that hold in each phase (for instance, describing mass conservation and heat diffusion) have to be solved. These equations are coupled by boundary conditions on the interface, such as the Stefan condition demanding energy balance and the Gibbs–Thomson equation [6,21,59]. Across the sharp interface, certain quantities (e.g., the heat flux, the concentration or the energy) may suffer jump discontinuities. The free-boundary (sharp-interface) description has been a successful model in a wide range of situations, but it also presents complications from the physical [2] and computational [15] points of view.

Phase-field models provide an alternative description for phase-transition phenomena. The phase-field method has been used to model foams [32], describe solidification processes [10,64], dendritic flow [49,53], microstructure evolution in solids [34], and liquid–liquid interfaces [61]. For recent reviews of phase-field methods the reader is referred to [16,30].

The key idea in phase-field models is to replace sharp interfaces by thin transition regions where the interfacial forces are smoothly distributed. Explicit front tracking is avoided by using smooth continuous variables locating grains or phase boundaries.

Phase-field models can be derived from classical irreversible thermodynamics [40]. Utilizing asymptotic expansions for vanishing interface thickness, it can be shown that classical sharp-interface models, including physical laws at interfaces and multiple junctions, are recovered [36,38]. In order to capture the physics of the problem, the transition regions (diffuse interfaces) in the phase-field models have to be extremely thin.

The use of diffuse-interface models to describe interfacial phenomena dates back to Korteweg [55] (1901), Cahn and Hilliard [12] (1958), Landau and Ginzburg [56] (1965) and van der Waals [74] (1979).

The Cahn–Hilliard phase-field model is normally used to simulate phase segregation of a binary alloy system, but many other applications, such as, image processing [23], planet formation [71] and cancer growth [33] are encountered in the literature.

1.2. Numerical methods for the Cahn–Hilliard phase-field model

1.2.1. Spatial discretization

The Cahn–Hilliard equation involves fourth-order spatial partial-differential operators. Traditional numerical methodologies for

* Corresponding author. Address: Group of Numerical Methods in Engineering, Department of Mathematical Methods, University of A Coruña, Campus de Elviña, 15192, A Coruña, Spain.
E-mail address: hgomez@ices.utexas.edu (H. Gómez).

0045-7825/$ - see front matter © 2008 Elsevier B.V. All rights reserved.
doi:10.1016/j.cma.2008.05.003

dealing with higher-order operators on very simple geometries include finite differences (see applications to the Cahn–Hilliard equation in [35,69]) and spectral approximations (solutions to the Cahn–Hilliard equation can be found in [58,60,78,79]). In real-world engineering applications, simple geometries are not very relevant, and therefore more geometrically flexible technologies need to be utilized. It is primarily this reason that has led to the finite element method being the most widely used methodology in engineering analysis. The primary strength of finite element methods has been in the realm of second-order spatial operators. The reason for this is variational formulations of second-order operators involve integration of products of first-derivatives. These are well defined and integrable if the finite element basis functions are piecewise smooth and globally $\mathscr{C}^0$-continuous, which is precisely the case for standard finite element functions. On the other hand, fourth-order operators necessitate basis functions that are piecewise smooth and globally $\mathscr{C}^1$-continuous. There are a very limited number of two-dimensional finite elements possessing $\mathscr{C}^1$-continuity applicable to complex geometries, but none in three-dimensions (see [68] for a recent study on $\mathscr{C}^1$-continuous finite elements). As a result, a number of different procedures have been employed over the years to deal with higher-order operators. All represent theoretical and computational complexities of one degree or another. Unfortunately, it may be said that after 50 years of finite element research, no general, elegant and efficient solution of the higher-order operator problem exists.

For the above reasons, finite element solutions to the Cahn–Hilliard equation are not common. The most common way to solve this equation in finite element analysis has been with mixed methods [4,5,9,24–26,31] rather than the use of $\mathscr{C}^1$-continuous function spaces [28]. Recently, a discontinuous Galerkin (DG) formulation has been proposed (see [77]). All of these methods lead to the introduction of extra degrees of freedom in addition to primal unknowns. As a consequence, an alternative approach is desirable. Perhaps, the most efficient procedure developed to date is the so-called continuous/discontinuous Galerkin (CDG) method [29,76]. In this method, standard $\mathscr{C}^0$-continuous finite element basis functions are used in conjunction with a variational formulation that maintains $\mathscr{C}^1$-continuity weakly through use of discontinuous Galerkin operators on derivatives. This eliminates extra degrees of freedom at the price of the inclusion of the discontinuous Galerkin operators which change the data structure from the normal one based solely on element interior contributions to one in which element edge or surface contributions are additionally required. Nevertheless, due to the reduction in degrees of freedom, this method seems to have the advantage over others previously proposed.

Recently, a new methodology, isogeometric analysis, has been introduced that is based on developments in computational geometry and computer aided design (CAD) [46]. Isogeometric analysis is a generalization of finite element analysis possessing several advantages: (1) It enables precise geometric definition of complex engineering designs thus reducing errors caused by low-order, faceted geometric approximation of finite elements. (2) It simplifies mesh refinement because even the coarsest model precisely represents the geometry. Thus, no link is necessary to the CAD geometry in order to refine the mesh, in contrast with the finite element method, in which each mesh represents a different approximation of the geometry. (3) It holds promise to simplify the mesh generation process, currently the most significant component of analysis model generation, and a major bottleneck in the overall engineering process. (4) The *k*-refinement process, unique to isogeometric analysis among geometrically flexible methodologies, has been shown to possess significant accuracy and robustness properties, compared with the usual *p*-refinement procedure utilized in finite element methods [3,20].

k-Refinement is a procedure in which the order of approximation is increased, as in the *p*-method, but continuity (i.e., smoothness) is likewise increased, in contrast to the *p*-method. Isogeometric analysis, thus, presents a unique combination of attributes that can be exploited on problems involving higher-order differential operators, namely, higher-order accuracy, robustness, two- and three-dimensional geometric flexibility, compact support, and, most importantly, $\mathscr{C}^1$ and higher-order continuity. In addition, higher-order continuity is achieved without introducing extra degrees of freedom. These properties open the way to application to phase-field models. Herein, we report our initial efforts to simulate higher-order operators using isogeometric analysis. Higher-order operators are encountered in biomedical applications and in many areas of engineering, such as, for example, liquid–liquid flows, liquid–vapor flows, emulsification, cancer growth, rotation-free thin shell theory, strain-gradient elastic and inelastic material models, and dynamic crack propagation, etc. The simplicity of isogeometric analysis compared with many procedures that have been published in the literature is noteworthy. We believe it may prove an effective procedure for solving problems of these kinds on complex geometries.

1.2.2. Time discretization

The time integration of the Cahn–Hilliard equation is not trivial. The non-linear fourth-order term imposes severe time-step size restrictions for explicit methods, thus mandating the use of implicit or (at least) semi-implicit algorithms. Under the non-realistic hypothesis that assumes the mobility to be constant, the fourth-order term of the Cahn–Hilliard equation becomes linear. One can take advantage of this fact by using a semi-implicit time integrator that treats the fourth-order term implicitly, while the non-linear second-order term is treated explicitly [43,79]. This technique allows a somewhat larger time step than explicit methods while avoiding the use of nonlinear solvers. However, in this paper we are interested in the thermodynamically relevant case, where the mobility depends on concentration and the fourth-order term is no longer linear. As a consequence, we will use a fully implicit time integration scheme which requires the use of a nonlinear solver.

Adaptive time stepping is of prime importance because the dynamic response of the Cahn–Hilliard equation intermittently experiences fast variations in time. The usual approach presented in the literature for simplified versions of the Cahn–Hilliard equation has been to use a few (2 or 3) different time-step sizes during the simulation [14]. These time steps are not selected by means of accuracy criteria, but by using approximate theories of the late-time behavior of the Cahn–Hilliard equation [75]. In this paper we propose an adaptive-in-time method where the time step is selected by using an accuracy criterion. This allows us to reduce the compute time by factors of hundreds while ensuring that sufficient time accuracy is achieved. (Another approach that has been used in the literature to speed up the solution is the use of multigrid methods [51,52], which is not pursued in this work.)

2. The strong form of the Cahn–Hilliard equation

Let $\Omega \subset \mathbb{R}^d$ be an open set, where $d = 2$ or 3. The boundary of Ω, assumed sufficiently smooth, is denoted Γ. The unit outward normal to Γ is denoted $\boldsymbol{n}$. We assume the boundary Γ is composed of two complementary parts, $\Gamma = \overline{\Gamma_g \cup \Gamma_s}$. A binary mixture is contained in Ω and c denotes the concentration of one of its components. The evolution of the mixture is assumed governed by the Cahn–Hilliard equation. In strong form, the problem can be stated as: find $c : \overline{\Omega} \times (0,T) \mapsto \mathbb{R}$ such that

$$\frac{\partial c}{\partial t} = \nabla \cdot (M_c \nabla(\mu_c - \lambda \Delta c)) \quad \text{in } \Omega \times (0,T), \tag{1.1}$$

$$c = g \quad \text{on } \Gamma_g \times (0,T), \tag{1.2}$$

$$M_c\nabla(\mu_c - \lambda\Delta c)\cdot\boldsymbol{n} = s \quad \text{on } \Gamma_s\times(0,T), \tag{1.3}$$
$$M_c\lambda\nabla c\cdot\boldsymbol{n} = 0 \quad \text{on } \Gamma\times(0,T), \tag{1.4}$$
$$c(\boldsymbol{x},0) = c_0(\boldsymbol{x}) \quad \text{in } \Omega. \tag{1.5}$$

where M_c is the mobility, μ_c represents the chemical potential of a regular solution in the absence of phase interfaces and λ is a positive constant such that $\sqrt{\lambda}$ represents a length scale of the problem. This length scale is related to the thickness of the interfaces that represent the transition between the two phases.

Remarks:

(1) In most of the existing analytic studies, as well as numerical simulations, the mobility is assumed to be constant. However, according to thermodynamics [11], it should depend on the mixture composition. This dependence might produce quite important changes of the coarsening kinetics. In this paper we consider the commonly adopted relationship.

$$M_c = Dc(1-c) \tag{2}$$

in which D is a positive constant which has dimensions of diffusivity, that is, length^2/time. This relationship appeared in the original derivation of the Cahn–Hilliard equation [11] and is commonly referred to as degenerate mobility, as pure phases have no mobility. We observe that relation (2) restricts the diffusion process primarily to the interfacial zones, which is precisely what happens in many physical situations where movement of atoms is confined to the interfacial region [11,63]. The reader is referred to the paper by Elliott and Garcke [27] for a proof of the existence of weak solutions of the Cahn–Hilliard equation with degenerate mobility. Further information about the regularity of the solutions can be found in [50]. Numerical simulations of the Cahn–Hilliard equation with degenerate mobility are reported on in [4,76,77].

(2) The function μ_c is a highly nonlinear function of the concentration representing the chemical potential of a uniform solution [12]. It is usually approximated by a polynomial of degree three. In this paper we consider the thermodynamically consistent function, namely:

$$\mu_c = \frac{1}{2\theta}\log\frac{c}{1-c} + 1 - 2c, \tag{3}$$

where $\theta = T_c/T$ is a dimensionless number which represents the ratio between the critical temperature T_c (the temperature at which the two phases attain the same composition) and the absolute temperature T.

2.1. The energy functional for the Cahn–Hilliard equation

An important feature of the Cahn–Hilliard model is the existence of an energy functional given by the Ginzburg–Landau free energy, namely

$$\mathscr{E}(c) = \int_\Omega (\Psi^c + \Psi^s)\mathrm{d}\boldsymbol{x}, \tag{4}$$

where Ψ^c is the chemical free energy and Ψ^s a surface free energy term. According to the original model of Cahn and Hilliard [12,13], the surface free energy is given by

$$\Psi^s = N\omega\frac{1}{2}\lambda\|\nabla c\|^2, \tag{5}$$

while the chemical free energy takes the form

$$\Psi^c = NkT(c\log c + (1-c)\log(1-c)) + N\omega c(1-c), \tag{6}$$

where N is the number of molecules per unit volume, k is Boltzmann's constant and ω is an interaction energy, which, for a system with a miscibility gap, is positive and is related to the critical temperature by

$$\omega = 2kT_c. \tag{7}$$

For $\theta = T_c/T > 1$, the chemical free energy is non-convex, with two wells, which drive phase segregation into the two binodal points (values of c that minimize the chemical free energy). For $\theta \leqslant 1$ it has a single well and admits a single phase only.

The chemical potential μ_c is given by $\mu_c = \Psi^{c'}/(N\omega)$, where $\Psi^{c'}$ is the derivative of Ψ^c with respect to c. Due to the complexity of the function Ψ^c, some simpler approximations are normally employed. In particular, a polynomial of degree four has been used to approximate the chemical free energy in most analytic studies and numerical simulations. The paper by Debussche and Detorri [22] (from the analytic point of view) and the papers by Wells et al. [76], Copetti et al. [19] and Xia et al. [77] (from the numerical point of view) deal with the issue of logarithmic free energy. In the present work we will use the logarithmic function given by (6).

Remarks:

(1) According to the Cahn–Hilliard model, the concentration is driven to the binodal points (those values of c that minimize the chemical free energy) and not to the pure phases.

(2) The energy functional given by (4) constitutes a Lyapunov functional since some simple manipulations lead to the inequality.

$$\frac{\mathrm{d}E}{\mathrm{d}t} = -\int_\Omega \nabla(-\lambda\Delta c + \mu_c)M_c\nabla(-\lambda\Delta c + \mu_c)\mathrm{d}\boldsymbol{x} \leqslant 0, \tag{8}$$

where E is a real-valued function defined as $E(t) = \mathscr{E}(c(\cdot,t))$.

2.2. Dimensionless form of the Cahn–Hilliard equation

In the numerical examples presented in this paper, we will use a dimensionless form of the Cahn–Hilliard equation. To derive the dimensionless equation, we introduce non-dimensional space and time coordinates

$$x^\star = x/L_0, \quad t^\star = t/T_0, \tag{9}$$

where L_0 is a representative length scale and $T_0 = L_0^4/(D\lambda)$. In the dimensionless coordinates, the Cahn–Hilliard equation becomes

$$\frac{\partial c}{\partial t^\star} = \nabla^\star\cdot\left(M_c^\star\nabla^\star(\mu_c^\star - \Delta^\star c)\right), \tag{10}$$

where $M_c^\star = c(1-c)$ and $\mu_c^\star = \mu_c L_0^2/\lambda$.

We will also make use of the dimensionless Ginzburg–Landau free energy given by

$$E^\star = \int_{\Omega^\star}\left(c\log c + (1-c)\log(1-c) + 2\theta c(1-c) + \frac{\theta}{3\alpha}\|\nabla^\star c\|^2\right)\mathrm{d}\boldsymbol{x}^\star, \tag{11}$$

where $E^\star = E(NkTL_0^3)^{-1}$ and

$$\alpha = \frac{L_0^2}{3\lambda} \tag{12}$$

is a dimensionless number related to the inverse of the thickness of the interfaces. The thickness of the interface is inversely proportional to $\alpha^{1/2}$.

Following [76], we will take the value $\theta = 3/2$ for the temperatures ratio (this corresponds to a physically relevant case). Therefore, the value of α completely characterizes our solutions.

Remark:

In what follows we will use the dimensionless form of the Cahn–Hilliard equation. For notational simplicity, we will omit the superscript stars henceforth.

3. Numerical formulation

3.1. Continuous problem in the weak form

We begin by considering a weak form for the Cahn–Hilliard equation. Let $\mathscr{V}$ denote the trial solution and weighting functions spaces, which are assumed to be identical. At this point we consider periodic boundary conditions in all directions. Therefore, the variational formulation is stated as follows: find $c \in \mathscr{V}$ such that $\forall w \in \mathscr{V}$,

$$B(w,c) = 0, \tag{13}$$

where

$$B(w,c) = \left(w, \frac{\partial c}{\partial t}\right)_\Omega + (\nabla w, M_c \nabla \mu_c + \nabla M_c \Delta c)_\Omega + (\Delta w, M_c \Delta c)_\Omega \tag{14}$$

and $(\cdot,\cdot)_\Omega$ is the $\mathscr{L}^2$ inner product with respect to the domain Ω. The space $\mathscr{V} = \mathscr{H}^2$ is a Sobolev space of square integrable functions with square integrable first and second derivatives.

The repeated integration by parts of Eq. (14) under the assumptions of periodic boundary conditions and sufficient regularity leads to the Euler–Lagrange form of (14):

$$\left(w, \frac{\partial c}{\partial t} - \nabla \cdot (M_c \nabla(\mu_c - \Delta c))\right)_\Omega = 0, \tag{15}$$

which implies the weak satisfaction of Eq. (10).

We refer to this formulation as the primal variational formulation.

3.2. The semidiscrete formulation

For the space discretization of (13) we make use of the Galerkin method. We approximate (13) by the following variational problem over the finite dimensional spaces: find $c^h \in \mathscr{V}^h \subset \mathscr{V}$ such that $\forall w^h \in \mathscr{V}^h \subset \mathscr{V}$

$$B(w^h, c^h) = 0, \tag{16}$$

where w^h and c^h are defined as

$$w^h = \sum_{A=1}^{n_b} w_A N_A, \tag{17}$$

$$u^h = \sum_{A=1}^{n_b} u_A N_A. \tag{18}$$

The N_A's are the basis functions, and n_b is the dimension of the discrete space. Note that the condition $\mathscr{V}^h \subset \mathscr{V}$ mandates our discrete space to be at least $\mathscr{H}^2$-conforming. This requirement is satisfied by a NURBS basis of $\mathscr{C}^1$-continuity or higher. In this paper we consider rectangular geometries. In this setting, three-dimensional NURBS reduce to simple B-splines in the usual tensor-product format [46]. An illustration of quadratic B-spline basis functions for an eight element mesh in one dimension is presented in Fig. 1. The functions are $\mathscr{C}^1$-continuous at knots and are $\mathscr{C}^\infty$-continuous elsewhere. Note that the functions are non-interpolatory at knots. As a result, the solution coefficients in (18), referred to as *control variables*, are not associated with the function value at nodes, as in conventional finite element analysis. In the variational methods literature they are sometimes referred to as *generalized coordinates*.

Remarks:

(1) The proposed spatial discretization can be applied to non-rectangular geometries while maintaining the same efficiency and simplicity of coding.
(2) One of the most promising ongoing extensions of the isogeometric concept is based on the use of T-Splines instead of NURBS. T-Splines were introduced by Sederberg [66] and represent a superset of NURBS. T-Splines retain the geometrical capabilities of NURBS, but allow for local refinement within a patch.

3.3. Time discretization and numerical implementation

We integrate in time using the generalized-α method. This method was originally derived in [18] for the equations of structural dynamics and subsequently applied to turbulence computations in [3,7,48]. In addition, we propose a time-step size predictor algorithm that allows us to compute three-dimensional stationary solutions in an affordable compute time.

3.3.1. Time-stepping scheme

Let $\boldsymbol{C}$ and $\dot{\boldsymbol{C}}$ denote the vector of degrees of freedom of concentration and concentration time derivative, respectively. We define the residual vector as

$$\boldsymbol{R} = \{R_A\}, \tag{19.1}$$

$$R_A = B(N_A, c^h). \tag{19.2}$$

The algorithm can be stated as: given $\dot{\boldsymbol{C}}_n, \boldsymbol{C}_n$ and $\Delta t_n = t_{n+1} - t_n$, find $\dot{\boldsymbol{C}}_{n+1}, \boldsymbol{C}_{n+1}, \dot{\boldsymbol{C}}_{n+\alpha_m}$ and $\boldsymbol{C}_{n+\alpha_f}$ such that

$$\boldsymbol{R}(\dot{\boldsymbol{C}}_{n+\alpha_m}, \boldsymbol{C}_{n+\alpha_f}) = 0, \tag{20.1}$$

$$\boldsymbol{C}_{n+1} = \boldsymbol{C}_n + \Delta t_n \dot{\boldsymbol{C}}_n + \gamma \Delta t_n (\dot{\boldsymbol{C}}_{n+1} - \dot{\boldsymbol{C}}_n), \tag{20.2}$$

$$\dot{\boldsymbol{C}}_{n+\alpha_m} = \dot{\boldsymbol{C}}_n + \alpha_m (\dot{\boldsymbol{C}}_{n+1} - \dot{\boldsymbol{C}}_n), \tag{20.3}$$

$$\boldsymbol{C}_{n+\alpha_f} = \boldsymbol{C}_n + \alpha_f (\boldsymbol{C}_{n+1} - \boldsymbol{C}_n). \tag{20.4}$$

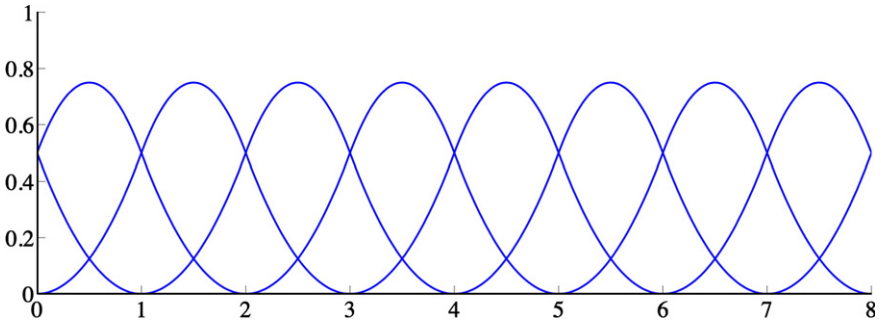

Fig. 1. One-dimensional $\mathscr{C}^1$-continuous quadratic periodic basis functions.

where Δt_n is the current time-step size and α_m, α_f and γ are real-valued parameters that define the method. Parameters α_m, α_f and γ are selected based on considerations of accuracy and stability. Taking $\alpha_m = \alpha_f = \gamma = 1$, the first order backward Euler method is obtained. Jansen, Whiting and Hulbert proved in [48] that, for a linear model problem, second-order accuracy in time is achieved if

$$\gamma = \frac{1}{2} + \alpha_m - \alpha_f \tag{21}$$

and unconditional stability is attained if

$$\alpha_m \geqslant \alpha_f \geqslant 1/2. \tag{22}$$

Parameters α_m, α_f can be parameterized in terms of ρ_∞, the spectral radius of the amplification matrix as $\Delta t \to \infty$, which controls high-frequency dissipation [45]:

$$\alpha_m = \frac{1}{2}\left(\frac{3-\rho_\infty}{1+\rho_\infty}\right), \quad \alpha_f = \frac{1}{1+\rho_\infty}. \tag{23}$$

Setting γ according to (21), a family of second-order accurate and unconditionally stable time integration schemes is defined in terms of the parameter $\rho_\infty \in [0,1]$. The nonlinear system of Eq. (20) is solved by using Newton's method, which leads to a two-stage predictor–multicorrector algorithm.

Predictor stage: Set

$$\boldsymbol{C}_{n+1,(0)} = \boldsymbol{C}_n, \tag{24.1}$$

$$\dot{\boldsymbol{C}}_{n+1,(0)} = \frac{\gamma-1}{\gamma}\dot{\boldsymbol{C}}_n. \tag{24.2}$$

where subscript 0 on the left-hand-side quantities denotes the iteration index of the non-linear solver. This predictor was shown to be efficient for turbulence applications [3,7,48].

Multicorrector stage: Repeat the following steps for $i = 1, 2, \ldots, i_{\max}$

(1) Evaluate iterates at the α-levels:

$$\dot{\boldsymbol{C}}_{n+\alpha_m,(i)} = \dot{\boldsymbol{C}}_n + \alpha_m(\dot{\boldsymbol{C}}_{n+1,(i-1)} - \dot{\boldsymbol{C}}_n), \tag{25.1}$$

$$\boldsymbol{C}_{n+\alpha_f,(i)} = \boldsymbol{C}_n + \alpha_f(\boldsymbol{C}_{n+1,(i-1)} - \boldsymbol{C}_n). \tag{25.2}$$

(2) Use these α-level iterates to assemble the residual and the tangent matrix of the linear system.

$$\boldsymbol{K}_{(i)}\Delta\dot{\boldsymbol{C}}_{n+1,(i)} = -\boldsymbol{R}_{(i)}. \tag{26}$$

Solve this linear system using a preconditioned GMRES algorithm (see Saad and Shultz [65]) to a specified tolerance.

(3) Use $\Delta\dot{\boldsymbol{C}}_{n+1,(i)}$ to update the iterates as

$$\dot{\boldsymbol{C}}_{n+1,(i)} = \dot{\boldsymbol{C}}_{n+1,(i-1)} + \Delta\dot{\boldsymbol{C}}_{n+1,(i)}, \tag{27.1}$$

$$\boldsymbol{C}_{n+1,(i)} = \boldsymbol{C}_{n+1,(i-1)} + \gamma\Delta t_n\Delta\dot{\boldsymbol{C}}_{n+1,(i)}. \tag{27.2}$$

This completes one non-linear iteration.

The tangent matrix in Eq. (26) is given by

$$\begin{aligned}\boldsymbol{K} &= \frac{\partial \boldsymbol{R}(\dot{\boldsymbol{C}}_{n+\alpha_m}, \boldsymbol{C}_{n+\alpha_f})}{\partial \dot{\boldsymbol{C}}_{n+\alpha_m}}\frac{\partial \dot{\boldsymbol{C}}_{n+\alpha_m}}{\partial \dot{\boldsymbol{C}}_{n+1}} + \frac{\partial \boldsymbol{R}(\dot{\boldsymbol{C}}_{n+\alpha_m}, \boldsymbol{C}_{n+\alpha_f})}{\partial \boldsymbol{C}_{n+\alpha_f}}\frac{\partial \boldsymbol{C}_{n+\alpha_f}}{\partial \dot{\boldsymbol{C}}_{n+1}} \\ &= \alpha_m \frac{\partial \boldsymbol{R}(\dot{\boldsymbol{C}}_{n+\alpha_m}, \boldsymbol{C}_{n+\alpha_f})}{\partial \dot{\boldsymbol{C}}_{n+\alpha_m}} + \alpha_f\gamma\Delta t_n \frac{\partial \boldsymbol{R}(\dot{\boldsymbol{C}}_{n+\alpha_m}, \boldsymbol{C}_{n+\alpha_f})}{\partial \boldsymbol{C}_{n+\alpha_f}}\end{aligned} \tag{28}$$

where the iteration index i has been omitted to simplify the notation.

Remarks:

(1) The value $\rho_\infty = 0.5$ has been shown to be an efficient choice for turbulence computations [7]. We adopted this value for all the computations presented in this paper.

(2) We used the consistent tangent matrix in our computations. Two to four nonlinear iterations are typically required to reduce the nonlinear residual to 10^{-4} of its initial value in a time step. The solution of system (26) to a tolerance of 10^{-4} requires normally 30–40 GMRES iterations using a diagonal preconditioner. The authors are currently working on the development of more efficient preconditioners.

3.3.2. Time-step size adaptivity

We borrowed ideas from embedded Runge–Kutta methods [8,41,73] to develop this algorithm. We took advantage of the fact that the generalized-α method becomes the backward Euler method when $\alpha_m = \alpha_f = \gamma = 1$. The adaptive time step strategy is presented in Algorithm 1. The formula we use to update the time-step size is

$$F(e, \Delta t) = \rho\left(\frac{\text{tol}}{e}\right)^{1/2}\Delta t \tag{29}$$

Our default values for the safety coefficient ρ and the tolerance tol are those suggested in [57], that is, $\rho = 0.9$ and $\text{tol} = 10^{-3}$.

The adaptive time stepping technique allows us to reduce the compute time by factors of hundreds compared to the compute time keeping the time-step size constant. Moreover, it provides an estimate of the time integration accuracy.

Remark:

When Algorithm 1 is used, the computed solution will be rejected and recomputed if the accuracy criterion is not fulfilled. Typically, fewer than 10% of the time steps are rejected using the safety coefficient $\rho = 0.9$.

Algorithm 1. Time step adaptive process

Given: $\boldsymbol{C}_n, \dot{\boldsymbol{C}}_n$ and Δt_n

Compute $\boldsymbol{C}^{\text{BE}}_{n+1}$ using backward Euler and Δt_n
Compute $\boldsymbol{C}^{\alpha}_{n+1}$ using second-order generalized-α and Δt_n
Calculate $e_{n+1} = \|\boldsymbol{C}^{\text{BE}}_{n+1} - \boldsymbol{C}^{\alpha}_{n+1}\|/\|\boldsymbol{C}^{\alpha}_{n+1}\|$
if $e_{n+1} > tol$ **then**
  Recalculate time-step size $\Delta t_n \leftarrow F(e_{n+1}, \Delta t_n)$
  goto 1
else
  Update time-step size $\Delta t_{n+1} = F(e_{n+1}, \Delta t_n)$
  continue
end if

4. Numerical results

In this section we investigate the performance of our spatial and temporal discretization strategies for the general Cahn–Hilliard model. We limit our studies to simple geometrical domains in an effort to focus our attention on the physical and numerical aspects of the problem. The domain of the test cases is a box $\Omega = (0,1)^d$, where $d = 2$ or 3. At the computational domain boundary, periodic boundary conditions are imposed in all directions. The spatial discretization is comprised of quadratic spline functions that are $\mathscr{C}^1$-continuous at knots. We employ meshes that are uniform in all directions.

The higher-order and higher-continuity spline basis functions allow the use of a Galerkin technique which yields a simple methodology. The efficiency, accuracy and robustness of the methodology enabled us to obtain the following results:

(1) Three-dimensional solutions for the general Cahn–Hilliard equation.
There are few published numerical results of the general case that we analyze in this paper. To our knowledge, only [76 and 77] report numerical solutions to this model, but the examples are limited to 2D domains and early times.

(2) Long-time behavior of the solution in three dimensions.The behavior of the stationary solutions in multidimensions is not well understood [1,14,17]. In most of the works reported on in the literature only the fast evolution of the concentration that takes place at the beginning of the segregation process is computed, so the coarsening process is completely neglected. This is due to the fact that the time integration of the Cahn–Hilliard equation is very time consuming and an efficient algorithm is necessary to be able to compute stationary solutions.
We remark that in our experience obtaining stationary solutions to the Cahn–Hilliard equation is much more challenging than computing only initial fast dynamics.

(3) Statistical studies of solutions with random initial conditions.The most commonly used initial condition for the Cahn–Hilliard equation is

$$c_0(\boldsymbol{x}) = \bar{c} + r, \tag{30}$$

where $\bar{c}$ is a constant (referred to as the volume fraction) and r is a random variable with uniform distribution. This fact makes difficult the comparison of solutions in terms of the Ginzburg–Landau free energy (the quantity that better describes the behavior of the solutions to the Cahn–Hilliard equation) because it is dependent on the initial condition. As a consequence, some statistics are necessary to compare numerical solutions. The statistics we consider in this work are the statistical moments up to order 10. The k-th order statistical moment is defined as,

$$M_k = \int_\Omega (c - \bar{c})^k \mathrm{d}\Omega \tag{31}$$

In the numerical examples, unless otherwise specified, r is a random variable with uniform distribution in $[-0.05, 0.05]$.

(4) A study of several values of the volume fraction.
Although the Cahn–Hilliard phase-field model was proposed five decades ago, there is still a lack of understanding of basic points. In particular, a study of simulations for several values of the volume fraction is lacking, even for the quartic chemical potential [70]. Studies of this kind are fundamental to understanding the model because the topology of solutions is strongly dependent on the volume fraction $\bar{c}$.

4.1. Numerical examples in two-dimensions

In this section we point out the main difficulties involved in computing solutions to the Cahn–Hilliard equation. We pay special attention to the computation of stationary solutions. We study the following issues:

(1) Convergence of the numerical solution under h-refinement.
(2) Dependence of the solution on the volume fraction $\bar{c}$.

4.1.1. Convergence of the numerical solution under h-refinement

We present two test cases which are defined by the sharpness parameter α and the volume fraction $\bar{c}$. We take the value $\bar{c} = 0.63$ in both cases. The sharpness parameter takes the values 3000 and 6000.

The initial condition is generated using Eq. (30). To perform the h-refinement study, the initial random distribution was generated on the coarsest mesh and then reproduced on the finer meshes. Thus, the initial condition is *exactly* the same on all meshes since the solution spaces are nested when the refinement is performed by knot insertion (see Hughes, Cottrell and Bazilevs [46]). The reason for doing this is that if the initial condition was generated by randomly perturbing control variables on each mesh, the Ginzburg–Landau energy would be significantly higher on the finer meshes, making the comparison of the energy on different meshes meaningless.

We will compare the solutions on the basis of statistical moments of order 2, 3 and 10 and the Ginzburg–Landau free energy.

(a) $\alpha = 3000$

We computed solutions on $32^2, 64^2$ and 128^2 meshes. The finer meshes are obtained from the coarser meshes by knot insertion [20,46]. Figs. 2–4 show, respectively, the evolution of the statistical

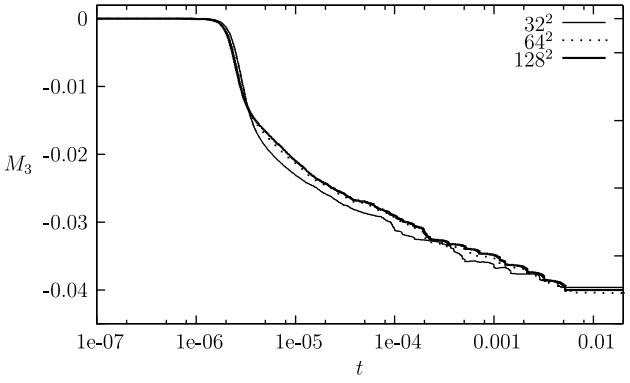

Fig. 3. Evolution of the third-order statistical moment of the concentration (M_3) for $\alpha = 3000$ and $\bar{c} = 0.63$.

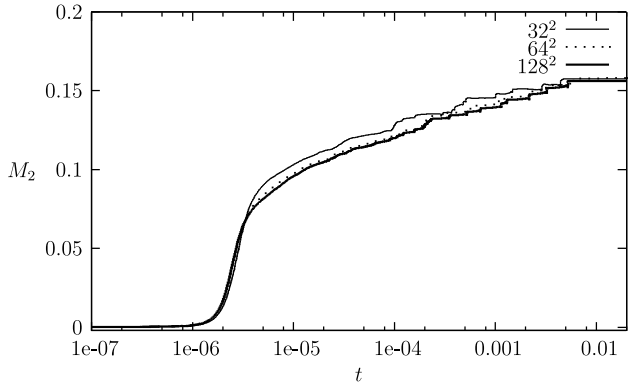

Fig. 2. Evolution of the second-order statistical moment of the concentration (M_2) for $\alpha = 3000$ and $\bar{c} = 0.63$.

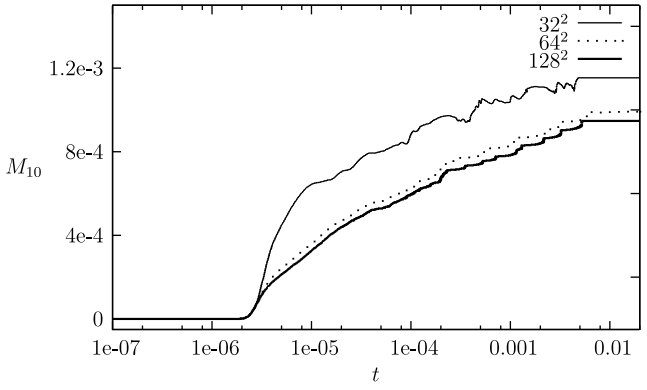

Fig. 4. Evolution of the tenth-order statistical moment of the concentration (M_{10}) for $\alpha = 3000$ and $\bar{c} = 0.63$.

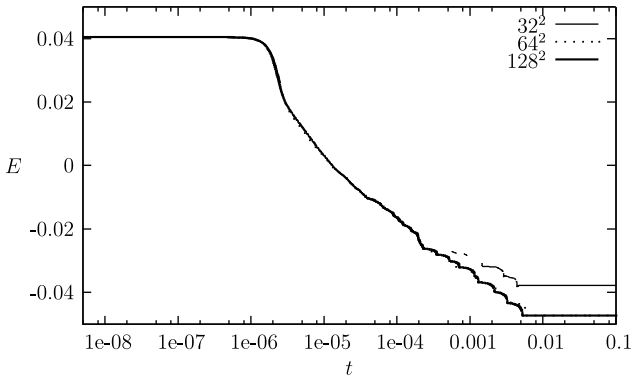

Fig. 5. Evolution of the Ginzburg–Landau free energy (E) for $\alpha = 3000$ and $\bar{c} = 0.63$.

moments of order 2, 3 and 10. The evolution of the free energy is depicted in Fig. 5. Figs. 2–5 show convergence under h-refinement. That is, given an initial condition, the evolution of the statistical moments and energy converges. The maximum difference in M_{10} between the 64^2 mesh and the 128^2 mesh is less than 5%, and the energy difference is barely discernible.

Fig. 6 shows snapshots of the solution computed on a 64^2 mesh (the results computed on a 128^2 mesh were indistinguishable from the 64^2 case, while the solution computed on a 32^2 mesh was significantly less accurate). We observe that the concentration is driven to the binodal points in a very fast process. The separation occurs approximately between the times $t = 2 \times 10^{-6}$ and $t = 4 \times 10^{-6}$ and is driven by the minimization of the chemical free energy Ψ^c. This explains the fast variation of the Ginzburg–Landau free energy that takes place in the time interval $(2 \times 10^{-6}, 4 \times 10^{-6})$ (see Fig. 5). After the phase separation, the coarsening process starts. The coarsening is driven by the minimization of the surface free energy Ψ^s. The representative time scales of the coarsening process are much larger than those of the separation process.

Remarks:

(1) Numerical solutions to this example can be found in [76 and 77] (the initial condition is identical in the statistical sense). In those references, the solution is computed on finer

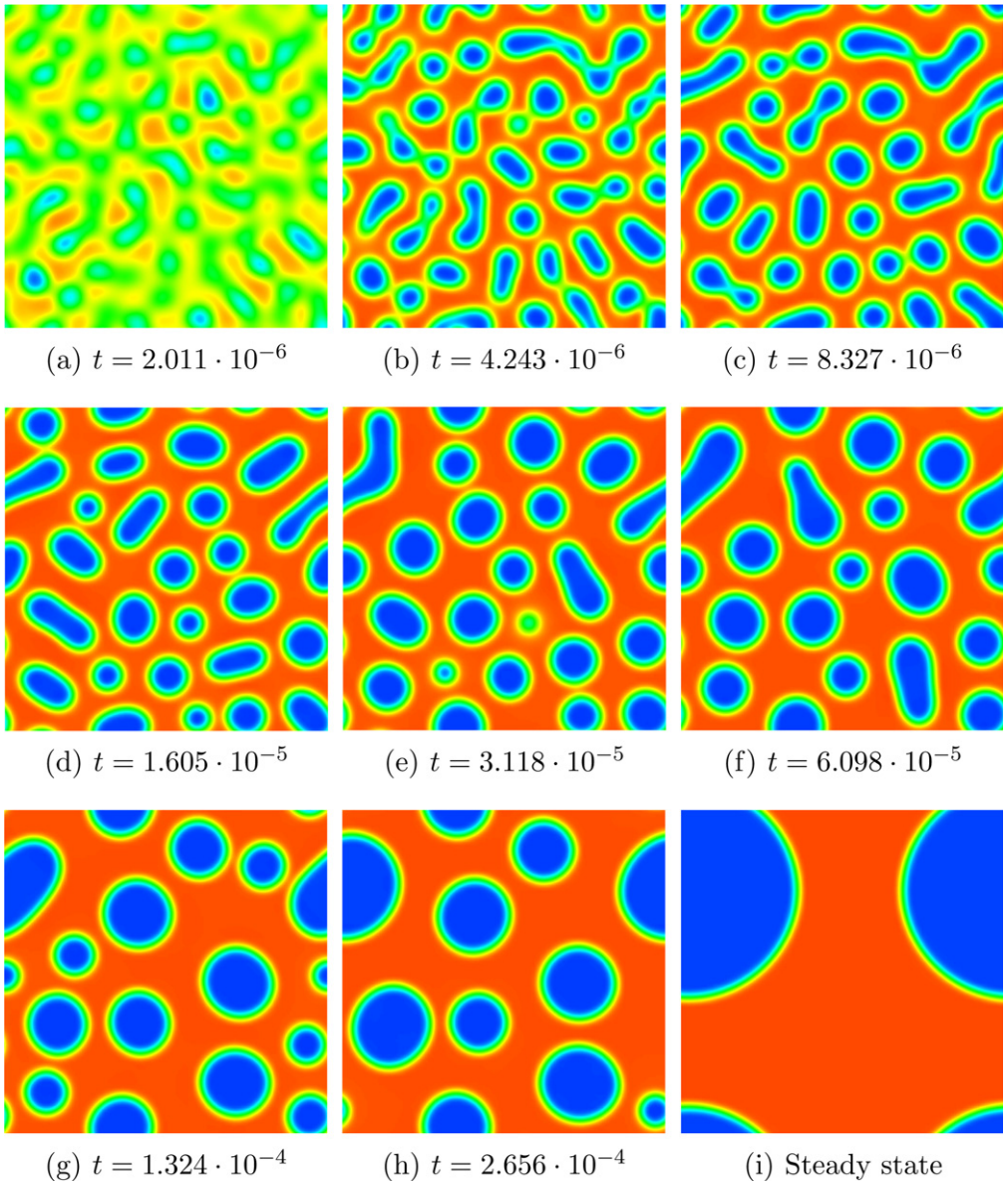

Fig. 6. Evolution of the concentration from a randomly perturbed initial condition for $\alpha = 3000$ and $\bar{c} = 0.63$. The mesh is comprised of 64^2 quadratic elements.

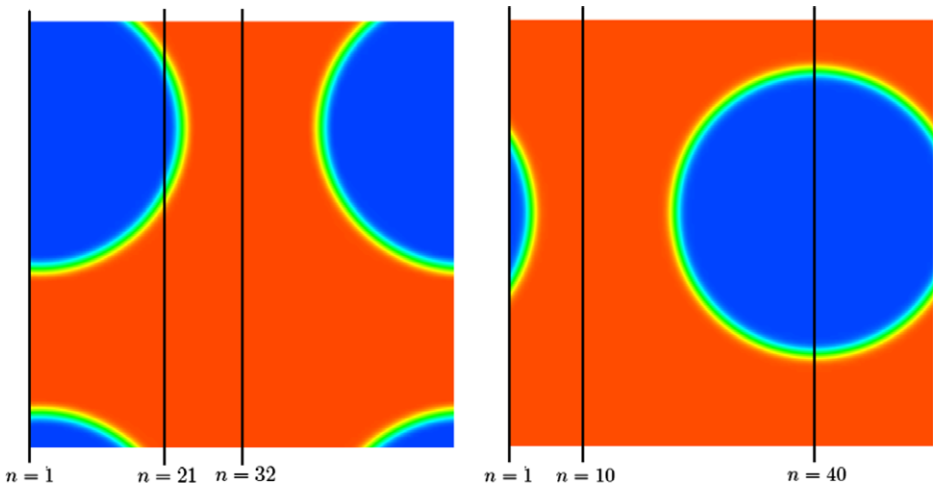

Fig. 7. Steady state solutions of the problem defined by $\alpha = 3000$ and $\bar{c} = 0.63$. In both pictures (left and right), the initial condition is the same from a statistical point of view, but not from a deterministic point of view. The mesh is comprised of 64^2 quadratic $\mathscr{C}^1$-continuous elements for the solution on the left hand side and 64^2 quartic $\mathscr{C}^3$-continuous elements for the solution on the right hand side. The vertical lines on the left and right hand side pictures represent the cutlines that have been plotted in Figs. 8 and 9, respectively.

meshes (80^2 linear elements in [77] and 10,283 quadratic elements in [76]). Additionally, in [77] the Cahn–Hilliard equation is reformulated as a five-equation system that results in a much larger number of degrees of freedom. In [76] the solution to this problem using mixed finite elements on a 80^2 mesh is also reported. This approach also requires the introduction of a number of additional degrees of freedom as compared to our method. Our solution computed on a mesh of 64^2 elements appears to be at least of equivalent quality to those reported on [76 and 77].

(2) The curve that corresponds to the 32^2 mesh in Fig. 5 is not defined for certain times. This is due to the fact the mesh was not fine enough for this problem and the numerical solution at those times was outside the physical range [0,1], the only interval where the energy is defined. (The authors anticipate using the Variational Multiscale Method [44,47] to address the numerical approximation of problems where the characteristic length scale of the equation is clearly unresolved by the computational mesh.)

(3) It is often argued that it is not possible to capture thin layers using high continuity basis functions. In this example a thin internal layer has been captured in an accurate and stable way using $\mathscr{C}^1$-continuous basis functions. In Fig. 8 we present cutlines of the steady solution for constant values of x corresponding to the vertical cutlines represented on the left hand side of Fig. 7. In Fig. 8, n and m represent the knot number in the x-direction and y-direction, respectively (see also Fig. 7). We sample the solution at knots and plot it using piecewise linear interpolation. The solution is monotone and the layer is captured within 4 elements. We also ran this example using $\mathscr{C}^3$-continuous quartic basis functions. For this case we were forced to use a different initial condition because the solution spaces are not nested when k-refinement is performed. In Fig. 9 we represent cutlines of the steady state solution for constant values of x (this corresponds to the vertical cutlines on the right hand side of Fig. 7).

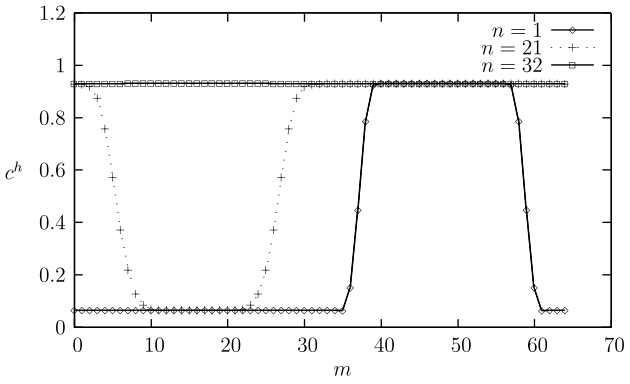

Fig. 8. Cutlines of the steady state solution using $\mathscr{C}^1$-continuous basis functions. The mesh is comprised of 64^2 quadratic elements. The problem is defined by $\alpha = 3000$ and $\bar{c} = 0.63$. The solution is sampled at mesh knots and plotted using linear interpolation. Symbols in the plot correspond to element boundaries. Note that despite high order and continuity of the basis functions, solutions are monotone and the sharp layers are captured within 4 elements.

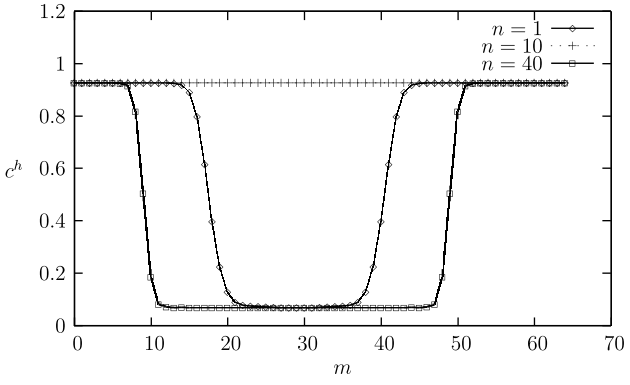

Fig. 9. Cutlines of the steady state solution using $\mathscr{C}^3$-continuous basis functions. The mesh is comprised of 64^2 quartic elements. The problem is defined by $\alpha = 3000$ and $\bar{c} = 0.63$. The solution is sampled at mesh knots and plotted using linear interpolation. Symbols in the plot correspond to element boundaries. Note that despite high order and continuity of the basis functions, solutions are monotone and the sharp layers are captured within 4–5 elements.

(b) $\alpha = 6000$

This test case is more challenging than the previous one, because the parameter α is larger. This means that the interfaces are thinner, which, in turn, requires a finer spatial mesh. In

addition, this case is more interesting from the physical point of view, since phase-field models tend to sharp-interface models as the thickness of the interfaces tends to zero.

We computed solutions on 64^2, 128^2 and 256^2 meshes. We plot snapshots of the solution computed on the 64^2 and 128^2 meshes. The results on the 256^2 mesh were indistinguishable from those on the 128^2 mesh.

In Figs. 10 and 11 we observe that the solutions at early and medium times on the 64^2 and 128^2 meshes are very similar. Only at the steady state do the solutions have significant differences. This example shows the difficulty involved in computing steady-state solutions to the Cahn–Hilliard equation. Obtaining stationary solutions is much more challenging than computing transient solutions at early and medium times not only from the point of view of the time integration, but also from the point of view of the spatial discretization.

The modification of the parameter α has not only changed the thickness of the interfaces, but it has also significantly modified the time scales of the problem. For example, the separation process is much faster for $\alpha = 6000$ than for $\alpha = 3000$.

Figs. 12–14 show the evolution of the statistical moments of order 2, 3 and 10, respectively. The evolution of the free energy has been depicted in Fig. 15. Figs. 12–15 demonstrate convergence under h-refinement.

Remarks:

(1) We investigated the possibility that the parameter *tol*, the tolerance used to estimate the time-step size, affected the results. We ran cases with $tol = 10^{-3}$ (our default value) and $tol = 10^{-4}$. We found no discernible differences in the computed statistics, while the time-step size was significantly smaller.

(2) We analyzed the performance of our time-step size predictor by running a simple case taking a constant time-step size $\Delta t = 10^{-9}$ (this was less than the minimal time-step size employed by our time integrator for that problem). We found no discernible differences in the computed statistics, which suggests that our adaptive time-stepping technique gives us very accurate solutions at a small fraction of the cost of the constant time-step strategy.

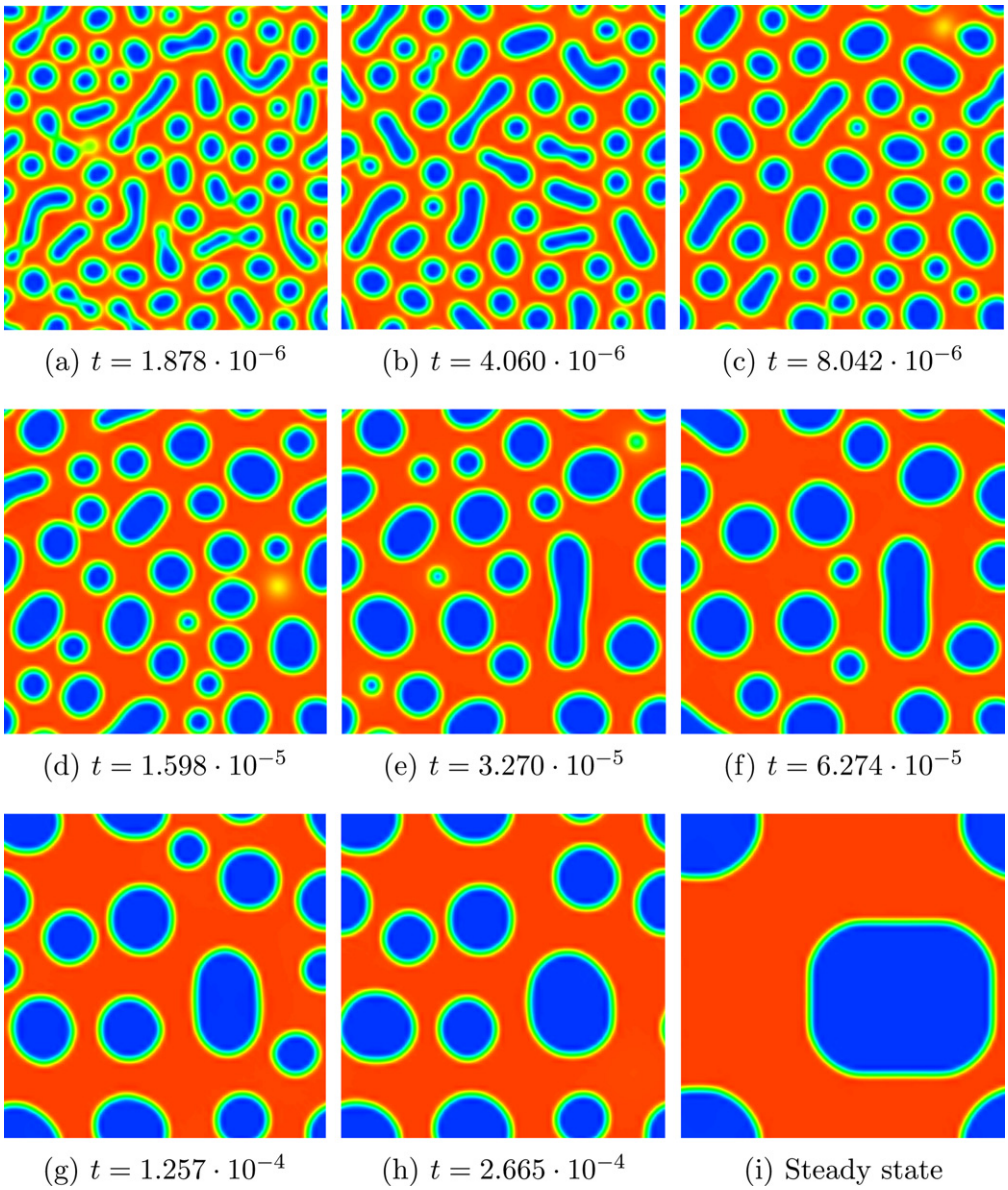

Fig. 10. Evolution of the concentration from a randomly perturbed initial condition for $\alpha = 6000$ and $\bar{c} = 0.63$. The mesh is comprised of 64^2 quadratic elements.

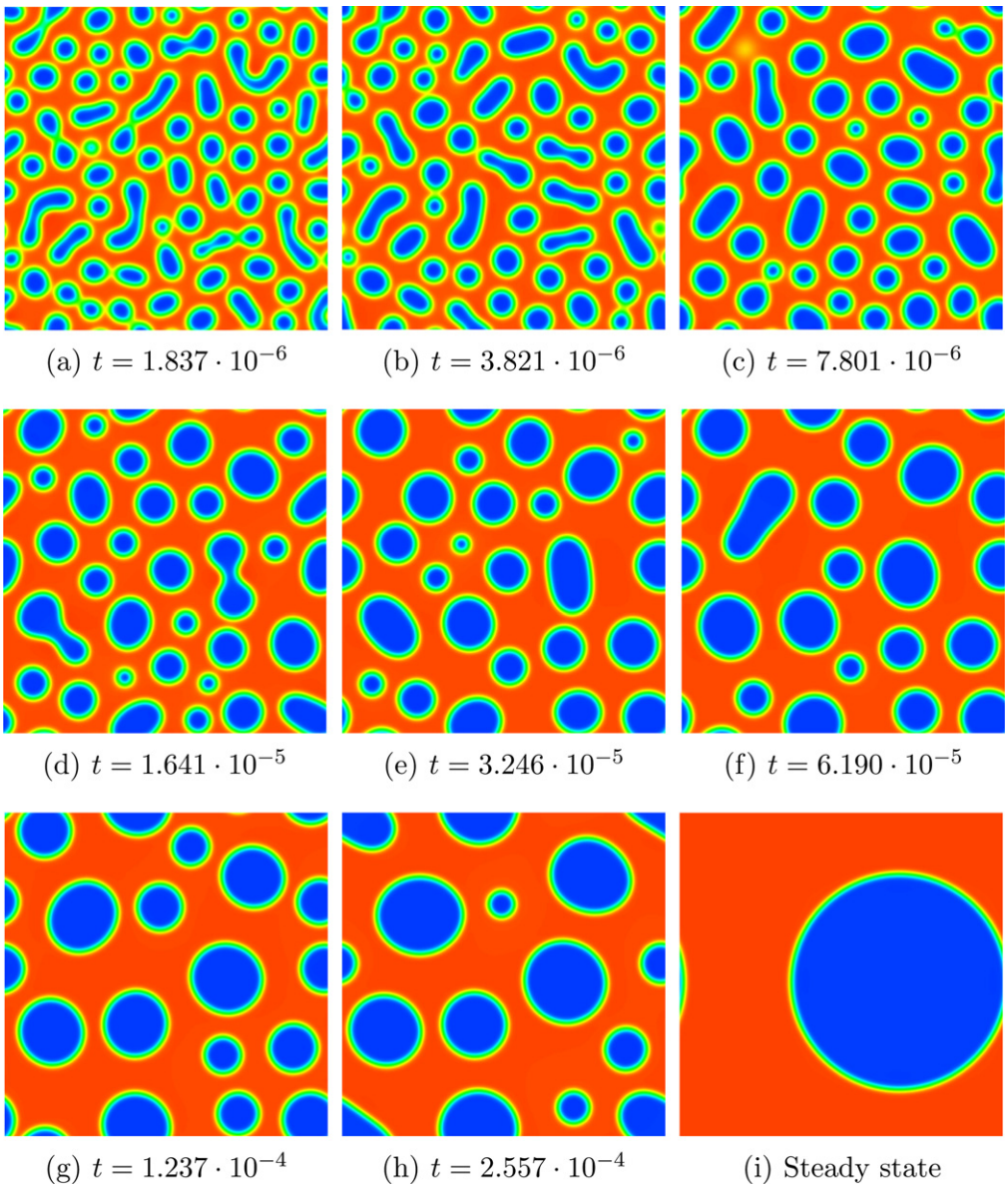

Fig. 11. Evolution of the concentration from a randomly perturbed initial condition for $\alpha = 6000$ and $\bar{c} = 0.63$. The mesh is comprised of 128^2 quadratic elements.

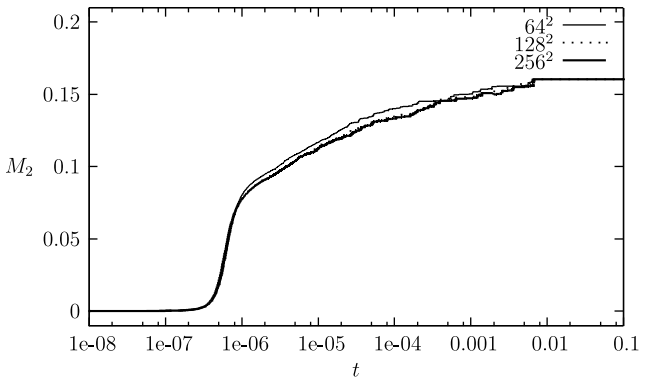

Fig. 12. Evolution of the second-order statistical moment of the concentration (M_2) for $\alpha = 6000$ and $\bar{c} = 0.63$.

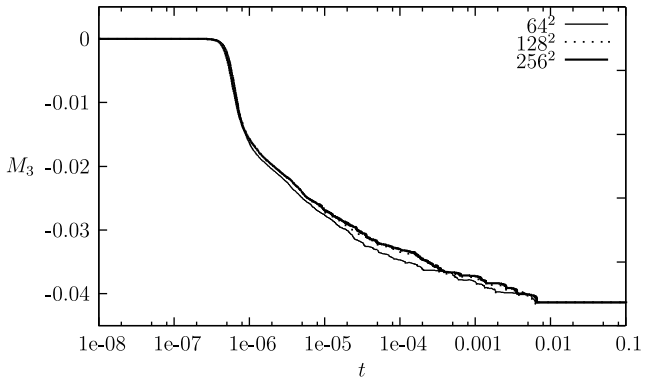

Fig. 13. Evolution of the third-order statistical moment of the concentration (M_3) for $\alpha = 6000$ and $\bar{c} = 0.63$.

(3) Our time-stepping strategy enabled us to integrate the equations in time up to $t \approx 10^{100}$, where the solutions were considered steady, at a reasonable computational cost. However, we plot the evolution of the Ginzburg–Landau free energy and the statistical moments only up to much earlier times in order to make the presentation clearer.

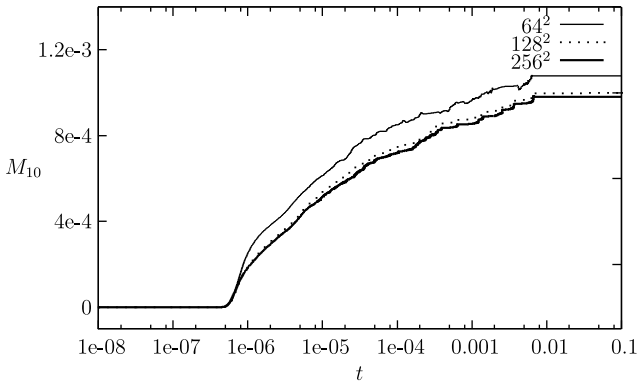

Fig. 14. Evolution of the tenth-order statistical moment of the concentration (M_{10}) for $\alpha = 6000$ and $\bar{c} = 0.63$.

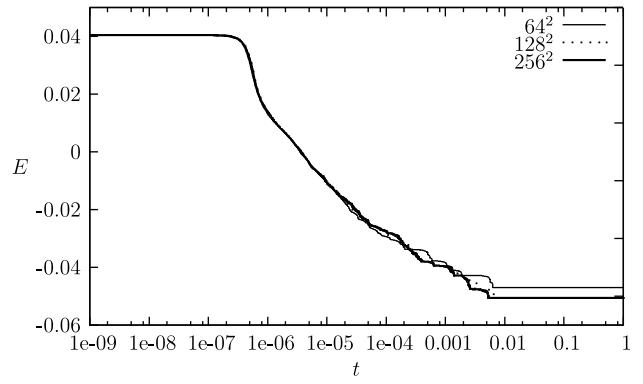

Fig. 15. Evolution of the Ginzburg–Landau free energy (E) for $\alpha = 6000$ and $\bar{c} = 0.63$.

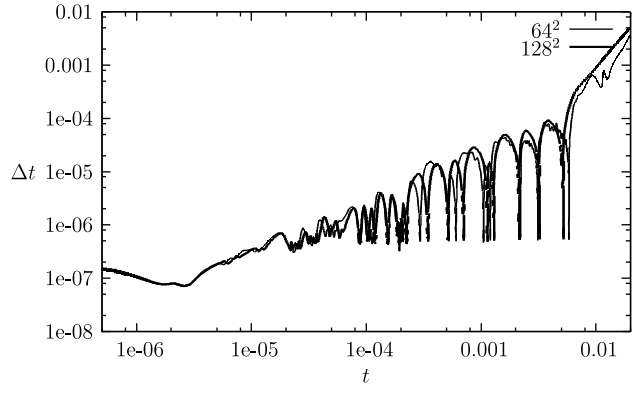

Fig. 16. Evolution of the time-step size on a doubly logarithmic plot for $\alpha = 3000$ and $\bar{c} = 0.63$.

(4) Most of the time-step size selection criteria that have been previously published are based on the free-energy decay. The fulfilment of inequality (8) at the discrete level is the condition more frequently asked for in Cahn–Hilliard simulations. In our experience, this is a very weak condition and the numerical solution can be completely wrong even if (8) is satisfied at the discrete level. Moreover, we found that the evolution of the energy is much more dependent on the spatial resolution rather than the temporal resolution.

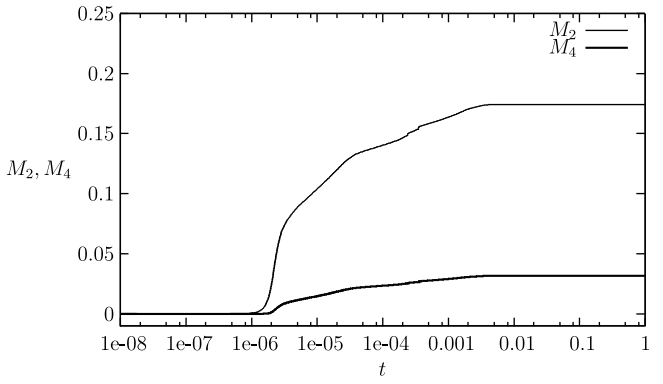

Fig. 17. Evolution of the second-order (M_2) and fourth-order (M_4) statistical moments of the concentration for $\alpha = 3000$ and $\bar{c} = 0.50$. The mesh is comprised of 128^2 quadratic elements.

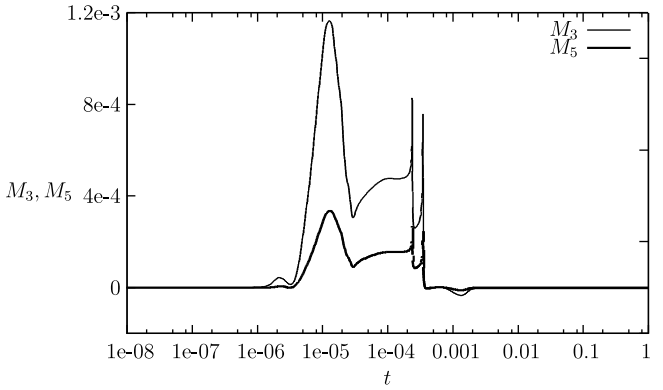

Fig. 18. Evolution of the third-order (M_3) and fifth order (M_5) statistical moments of the concentration for $\alpha = 3000$ and $\bar{c} = 0.50$. The mesh is comprised of 128^2 quadratic elements.

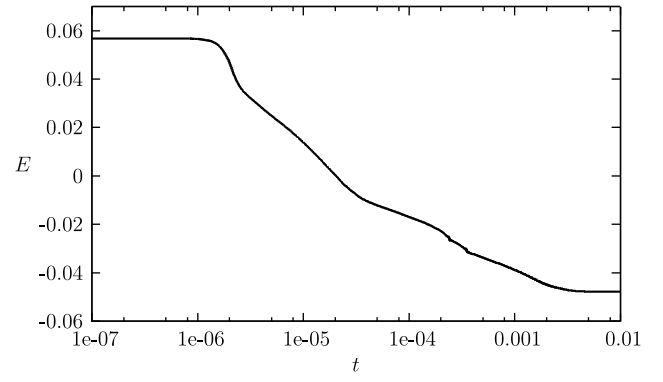

Fig. 19. Evolution of the Ginzburg–Landau free energy for $\alpha = 3000$ and $\bar{c} = 0.50$. The mesh is comprised of 128^2 quadratic elements.

(5) The time-step size predicted by our method is fairly independent of the spatial mesh. We plot in Fig. 16 the evolution of the time-step size for the simulation of the problem defined by $\alpha = 3000$ and $\bar{c} = 0.63$ on two different meshes. A similar behavior can be observed. Also, it is an instructive exercise to compare the evolution of the time-step size (Fig. 16) with the evolution of the Ginzburg–Landau free

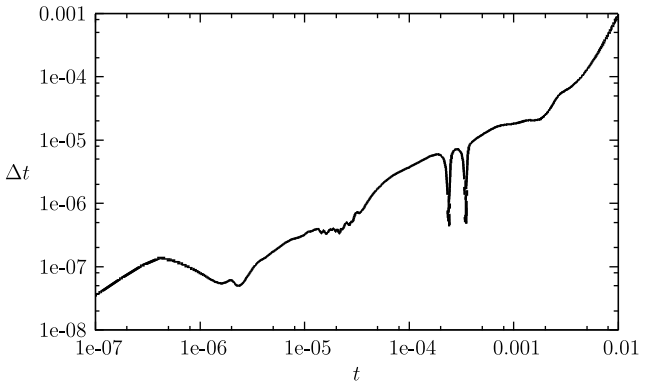

Fig. 20. Evolution of the time-step size on a doubly logarithmic plot for $\alpha = 3000$ and $\bar{c} = 0.50$. The mesh is comprised of 128^2 quadratic elements.

energy (Fig. 15). We observe that the separation process (identified in the energy plot by the fast variation in the temporal interval $[2 \times 10^{-6}, 4 \times 10^{-6}]$) is computed using very small time-step sizes. After the separation process is finished, the coarsening process starts. The coarsening takes place at much larger time scales, what is reflected by our time-step size predictor. Finally, we relate the fast variations of the time-step size in the last part of the simulation, $t \in [2 \times 10^{-4}, 4 \times 10^{-2}]$ to the rough variations of the free energy that take place at those times, which we conjecture is due to coalescence of bubbles.

(6) We use Gauss quadrature in all cases. We ran some of the test cases using three and four integration points per element in each direction. The computed statistics were indistinguishable.

(7) Low-order statistical moments are not good discriminators in most of the cases, while higher-order moments are, as M_{10} illustrates in Figs. 4 and 14. The Ginzburg–Landau free energy is the most informative quantity for comparing solutions at steady state, since the stationary solution can be defined as the one that minimizes the energy functional. However, the energy at short and medium times depends on the initial condition, which makes use of statistical moments necessary.

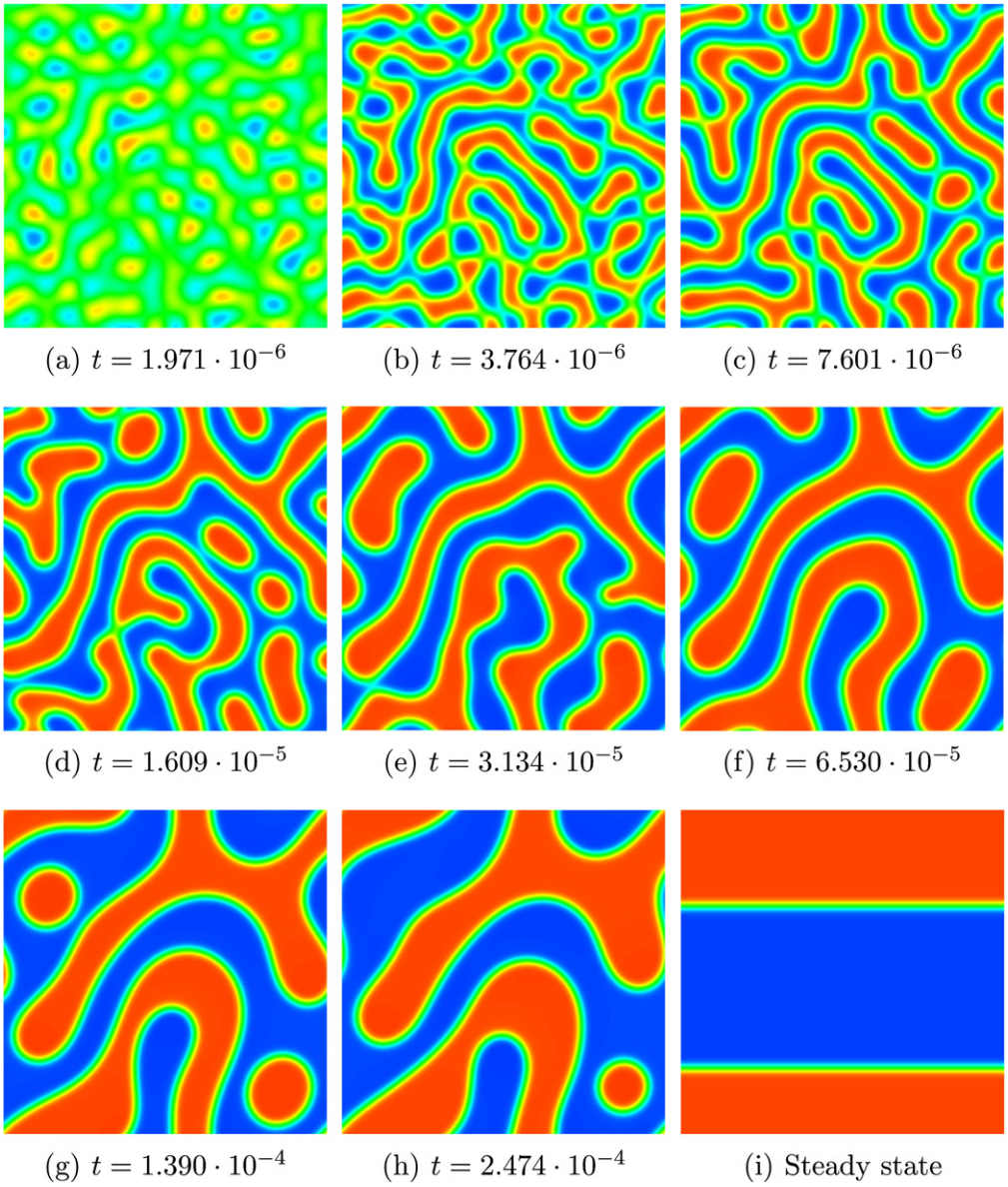

Fig. 21. Evolution of the concentration from a randomly perturbed initial condition for $\alpha = 3000$ and $\bar{c} = 0.50$. The mesh is comprised of 128^2 quadratic elements.

(8) We ran examples with different distributions for the random variable r. The distributions were uniform in $[-L, L]$, where $L = 5 \times 10^{-2}$ (our default value), $L = 5 \times 10^{-4}$ and $L = 5 \times 10^{-5}$. In the first two cases, although the statistics were different, we found similar dynamical processes. There was no phase separation for the case $L = 5 \times 10^{-5}$. In our experience it is very important that the pseudo-random number generator is statistically reliable. We recommend that standard tests [54] be used to verify its quality.

(9) We ran the previous examples on the domain $\Omega = (0, 2)^2$ to study the dependence of the solution on the size of the domain. The computed statistics were very similar.

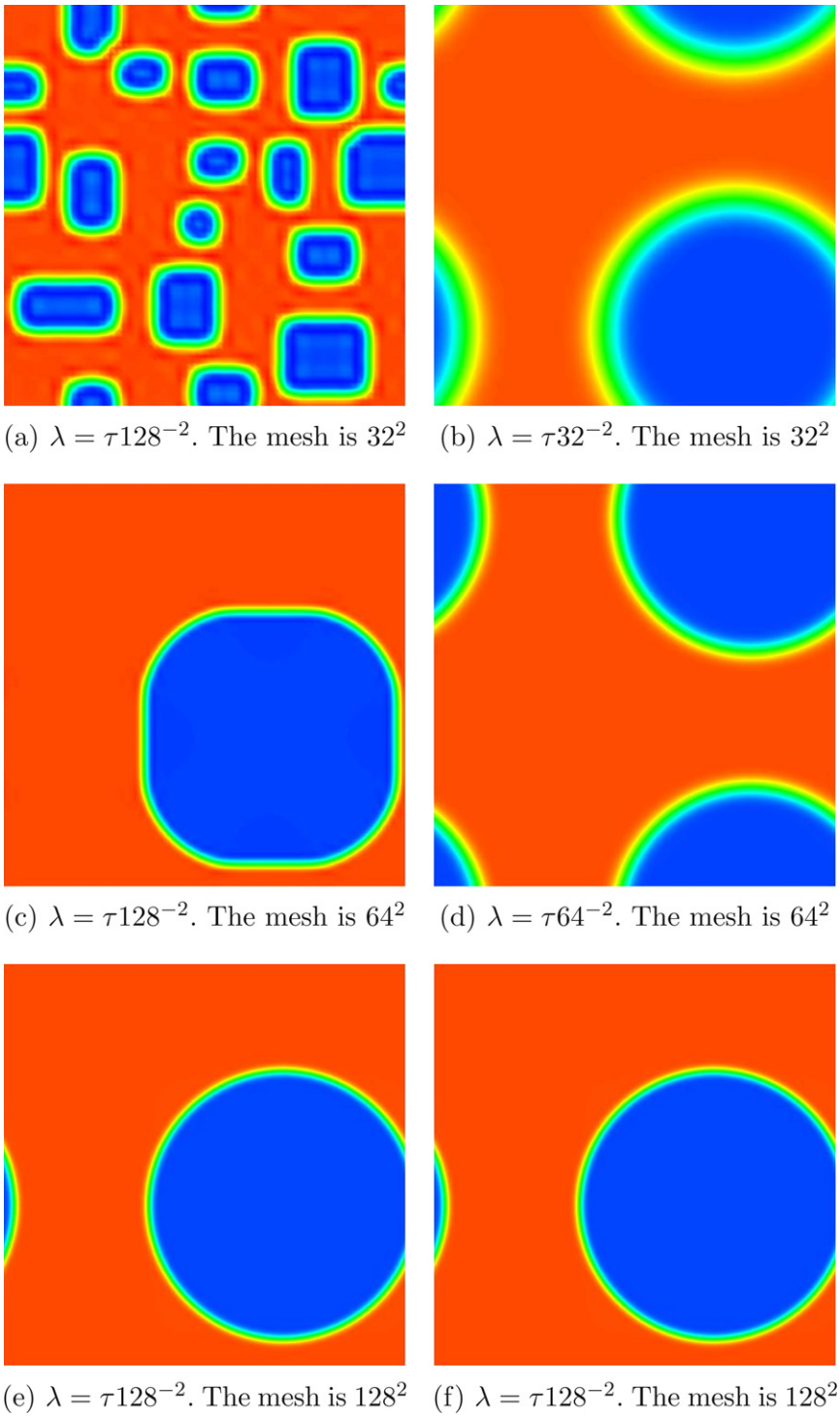

(a) $\lambda = \tau 128^{-2}$. The mesh is 32^2 (b) $\lambda = \tau 32^{-2}$. The mesh is 32^2

(c) $\lambda = \tau 128^{-2}$. The mesh is 64^2 (d) $\lambda = \tau 64^{-2}$. The mesh is 64^2

(e) $\lambda = \tau 128^{-2}$. The mesh is 128^2 (f) $\lambda = \tau 128^{-2}$. The mesh is 128^2

Fig. 22. Steady state solutions to the problem defined by $\bar{c} = 0.63$. We show the solutions on uniform meshes comprised of 32^2 (a)–(b), 64^2 (c)–(d) and 128^2 (e)–(f) quadratic elements. On the left hand side we plot the solution using $\lambda = \tau 128^{-2}$ for all meshes with $\tau = 1$. The dependence of the solution on the mesh size h is apparent. On the right hand side we plot the solutions adapting λ to the resolution of the computational mesh. The topology of the solution is invariant with respect to the mesh size. The only difference in the solutions on the right hand side is the thickness of the interface.

4.1.2. Dependence of the solution on $\bar{c}$

We present the numerical solution to the case defined by $\bar{c} = 0.50$ and $\alpha = 3000$. The mesh is comprised of 128^2 quadratic elements. We plot the evolution of the statistical moments of order 2 and 4 (Fig. 17) and 3 and 5 (Fig. 18). The evolution of the Ginzburg–Landau free energy is depicted in Fig. 19. We present snapshots of the solution in Fig. 21.

This solution presents two main differences as compared to those reported in the previous section:

(1) The topology of the solution is different than for the case $\bar{c} = 0.63$. This is the typical topology corresponding to $\bar{c} = 0.50$. A deeply interconnected pattern is characteristic of this topology. In the cases presented in Section 4.1.1

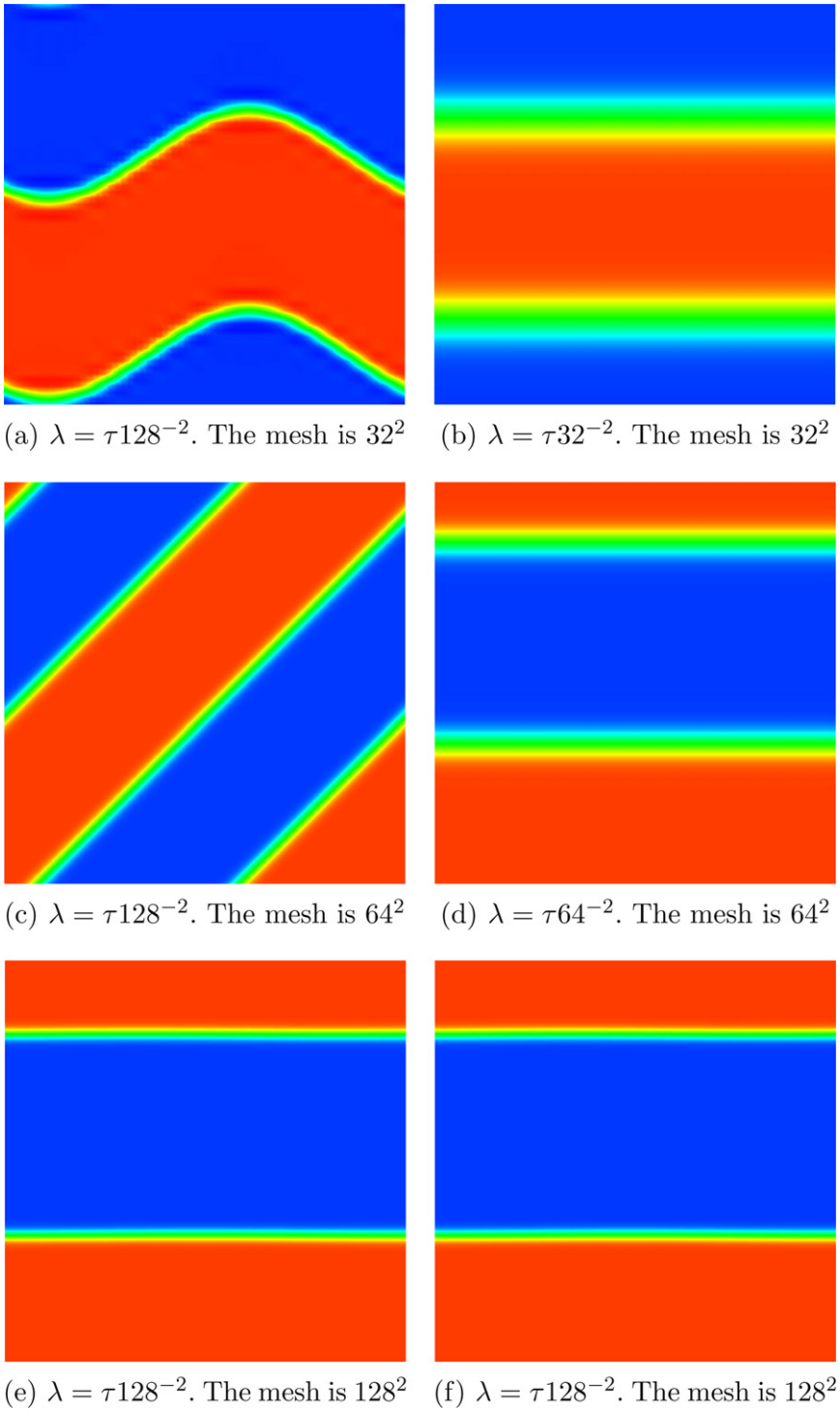

Fig. 23. Steady state solution to the problem defined by $\bar{c} = 0.50$. We show the solutions on uniform meshes comprised of 32^2 (a)–(b), 64^2 (c)–(d) and 128^2 (e)–(f) quadratic elements. On the left hand side we plot the solution using $\lambda = \tau 128^{-2}$ for all meshes with $\tau = 2.5$. The dependence of the solution on the mesh size h is apparent. On the right hand side we plot the solutions adapting λ to the resolution of the computational mesh. The topology of the solution is invariant with respect to the mesh size. The only difference in the solutions on the right hand side is the thickness of the interface.

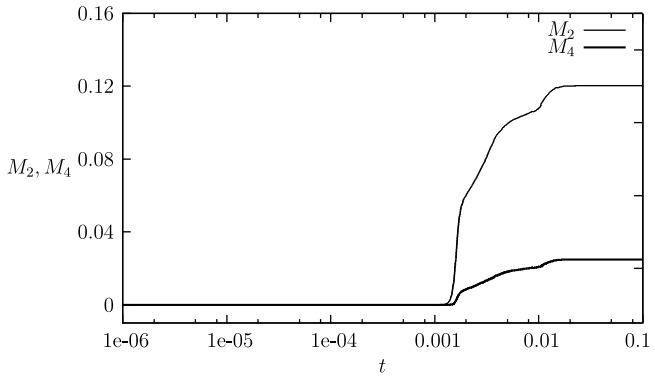

Fig. 24. Evolution of the second-order (M_2) and fourth-order (M_4) statistical moments of the concentration for $\alpha = 200$ and $\bar{c} = 0.63$. The mesh is comprised of 128^3 quadratic elements.

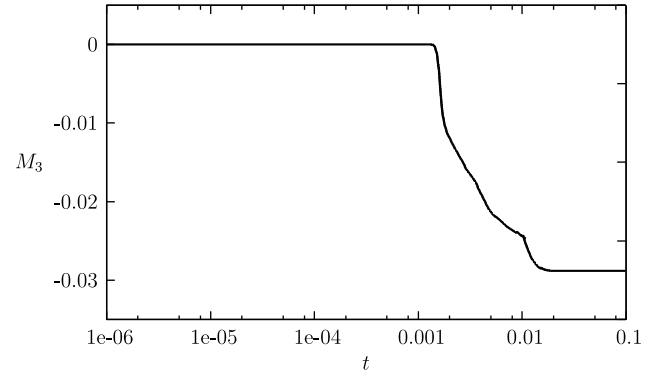

Fig. 25. Evolution of the third-order statistical moment of the concentration (M_3) for $\alpha = 200$ and $\bar{c} = 0.63$. The mesh is comprised of 128^3 quadratic elements.

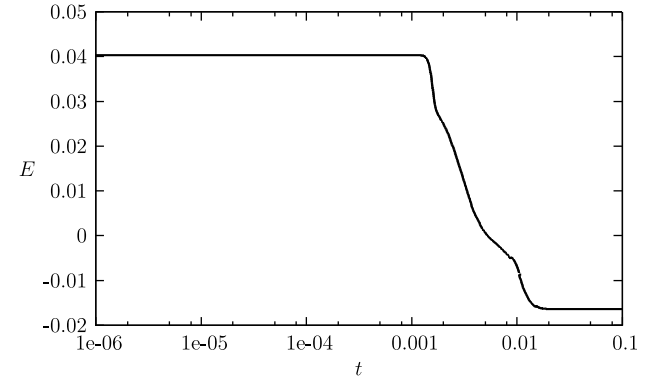

Fig. 26. Evolution of the Ginzburg–Landau free energy (E) for $\alpha = 200$ and $\bar{c} = 0.63$. The mesh is comprised of 128^3 quadratic elements.

the masses of the two phases were substantially different ($\bar{c} = 0.63$ and $1 - \bar{c} = 0.37$), which leads to the phenomenon of nucleation. In this case, one finds irregular droplets that evolve to circular shapes whose characteristic length increases with time [39]. Also, we observe that the energy plot is smoother for $\bar{c} = 0.50$ than for $\bar{c} = 0.63$. This is due to the fact that the coarsening process is more continuous for this case, as a consequence of the absence of nucleation.

(2) In the case $\bar{c} = 0.50$ the exact solution at the steady state is a strip instead of a circle. Geometrical arguments support this. Further discussion about this point will be presented in the sequel.

In Fig. 20 we present the evolution in time of the time-step size for this case, which is significantly different than that in Fig. 16. The reason is, again, the different topology of the solution. In the case defined by $\bar{c} = 0.50$ there is no nucleation and, as a consequence, the coarsening process is more continuous, which is reflected by our time-step size predictor (compare Fig. 16 with Fig. 20). This fact can also be observed in the plot of the Ginzburg–Landau free energy (Fig. 19) which is significantly smoother than that of Fig. 5. The only sign of nucleation is observed in the (g) and (h) snapshots of Fig. 21, corresponding to local minima in the time-step size plot (Fig. 20) and with small but rapid variations in the Ginzburg–Landau free energy (see Fig. 19).

4.1.3. Topology of the steady-state solution and the isoperimetric problem

The interest in stationary solutions to the Cahn–Hilliard equation (besides the multiple applications of this model in material science) is its relation with the periodic isoperimetric problem [42], which is one of the major open problems in geometry. It was shown in [62,67] that minimizers of the Ginzburg–Landau free energy (under an appropriate rescaling) converge to solutions of the isoperimetric problem when $\alpha \to \infty$ and $\theta \to \infty$.

In a 2D periodic square (2D flat torus) the solution of the periodic isoperimetric problem is well known: the minimizers are either a circle (when $0 < \bar{c} \leqslant 1/\pi$ or $1 - 1/\pi \leqslant \bar{c} \leqslant 1$) or a strip (when $1/\pi \leqslant \bar{c} \leqslant 1 - 1/\pi$) but in 3D the periodic isoperimetric problem remains open even in a periodic cube.[1]

The 2D solutions to the periodic isoperimetric problem (a circle and a strip) correspond to the solutions that we obtained for $\bar{c} = 0.63$ (circle) and $\bar{c} = 0.50$ (strip). These solutions were obtained for $\alpha = 3000$ and $\alpha = 6000$ in the case of the circle and for $\alpha = 3000$ in the case of the strip. In all cases $\theta = 3/2$.

According to the results quoted for the isoperimetric problem, the case given by $\bar{c} = 0.63$, although close to the limit value $1 - 1/\pi$, corresponds to a strip, while the computed solution for the Cahn–Hilliard equation is a circle. This is due to θ not being large enough. Increasing θ drives the binodal points closer to the pure phases. In this case, the strip is an energetically better solution than the circle. We feel it is important that our solutions correspond to solutions of the periodic isoperimetric problem. This link is relevant to discriminate between physically acceptable and unacceptable solutions.

Remark:

If the Cahn–Hilliard phase-field model is to be used for the approximation of solutions of the isoperimetric problem, the authors recommend the use of constant mobility and quartic chemical potential, which also converges to solutions of the isoperimetric problem as $\alpha \to \infty$, but requires a significantly smaller compute time.

4.1.4. Mesh-independent Cahn–Hilliard phase-field model

The Cahn–Hilliard phase-field model converges, in a thermodynamically consistent fashion, to its corresponding sharp-interface model as $\sqrt{\lambda}$ (the characteristic length scale of the model) tends to zero. In order for the Cahn–Hilliard phase-field model to be realistic for engineering applications, λ has to be extremely small. On the other hand, if the computational mesh is not fine enough to

[1] It has been conjectured that the possible solutions are a sphere, a cylinder and two parallel planes.

resolve the internal layers whose size is defined by the length scale $\sqrt{\lambda}$, non-physical solutions are obtained.

To desensitize this mesh dependence, we propose to relate the characteristic length scale of the continuous phase-field model to the characteristic length scale of the computational mesh. In the ideal case we would obtain the best approximation to the sharp-interface model for a given mesh. Also, we are seeking a method that preserves the topology of the solution at the steady state independently of the mesh size while the thickness of the interface is enlarged according to the spatial resolution. Numerical results using

$$\lambda = \tau h^2, \tag{32}$$

where τ is a dimensionless constant, have shown the potential of this approach. The value of τ has been determined by means of numerical examples. It turned out that the maximum value of τ that

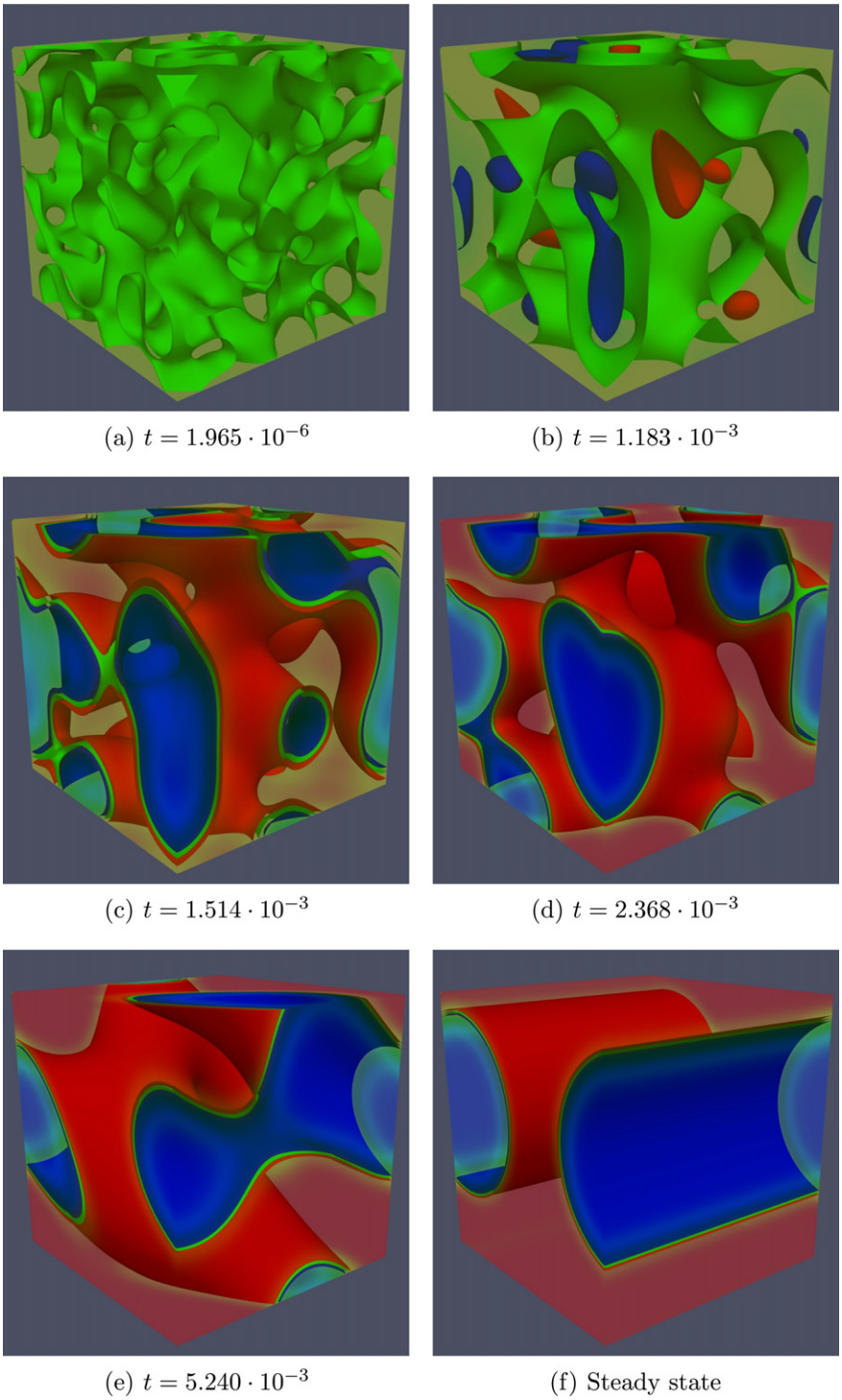

Fig. 27. Evolution of the concentration from a randomly perturbed initial condition for $\alpha = 200$ and $\bar{c} = 0.63$. The mesh is comprised of 128^3 quadratic elements. (a) $t = 1.965 \times 10^{-6}$, (b) $t = 1.183 \times 10^{-3}$, (c) $t = 1.514 \times 10^{-3}$, (d) $t = 2.368 \times 10^{-3}$, (e) $t = 5.240 \times 10^{-3}$ and (f) steady state.

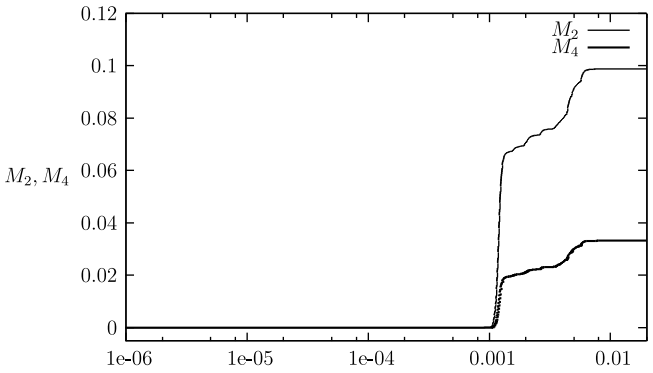

Fig. 28. Evolution of the second-order (M_2) and third-order (M_3) statistical moments of the concentration for $\alpha = 600$ and $\bar{c} = 0.75$. The mesh is comprised of 128^3 quadratic elements.

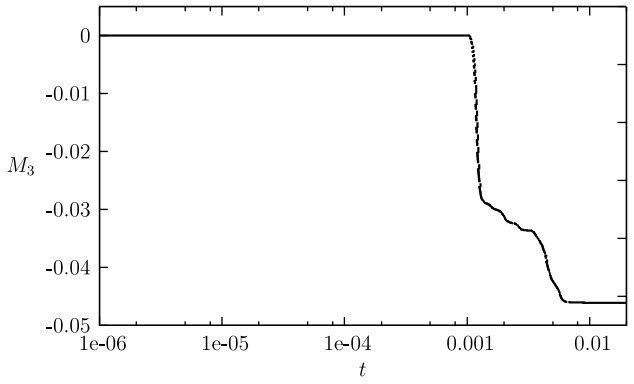

Fig. 29. Evolution of the third-order statistical moment of the concentration (M_3) for $\alpha = 600$ and $\bar{c} = 0.75$. The mesh is comprised of 128^3 quadratic elements.

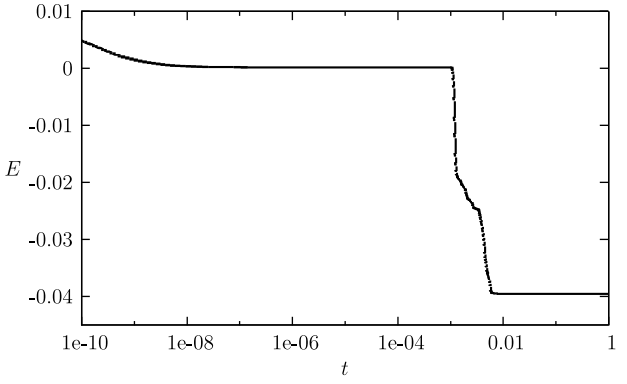

Fig. 30. Evolution of the Ginzburg–Landau free energy (E) for $\alpha = 600$ and $\bar{c} = 0.75$. The mesh is comprised of 128^3 quadratic elements.

can be used retaining mesh invariance depends on the average concentration $\bar{c}$. The closer $\bar{c}$ is to 0.5 the larger τ has to be and, consequently, the thicker the interface. We show examples using $\tau = 1$ for $\bar{c} = 0.63$ and $\tau = 2.5$ for $\bar{c} = 0.50$. The results are encouraging.

In the first example, $\bar{c} = 0.63$. In Fig. 22 we show the solutions on uniform meshes comprised of $32^2, 64^2$ and 128^2 quadratic elements. The initial condition is generated by randomly perturbing control variables on the 32^2 mesh and then it is exactly reproduced on the finer meshes as in the previous numerical examples. On the left hand side, we plot the solution using for all meshes $\lambda = \tau 128^{-2}$ where $\tau = 1$. We find a strong dependence of the solution on the mesh size. On the right hand side we plot the solution adapting λ to the resolution of the computational mesh through use of Eq. (32) with $\tau = 1$. In this case, the topology of the numerical solution is independent of the mesh size and the interface is captured on all meshes within 4–5 elements.

In the second example, $\bar{c} = 0.5$. In Fig. 23 we show the solution on uniform meshes comprised of $32^2, 64^2$ and 128^2 quadratic elements. The initial condition is generated in the same way as in the previous example. The solutions on the left hand side have been computed using $\lambda = \tau 128^{-2}$ for all meshes with $\tau = 2.5$. A strong dependence of the solution on mesh size is observed. The solutions on the right hand side of Fig. 23 have been computed adapting λ to the resolution of the computational mesh using Eq. (32) and $\tau = 2.5$. The topology of the numerical solution is again invariant with respect to the mesh size and the interface is captured on all meshes within 4–5 elements.

The previous examples show the potential of the proposed approach to successfully deal with problems where the characteristic length scale of the continuous phase-field model is unresolved by the computational mesh. We believe that with this technique phase-field modeling, which has been used heretofore primarily in scientific studies, may become a practical engineering technology.

4.2. Numerical examples in three-dimensions

The complexity involved in the approximation of a 3D solution to the Cahn–Hilliard equation is much greater than for the 2D problem. The topology of the solution is much more complex and it experiences significant changes as time evolves. There seems to be almost nothing known about the steady state solutions in 3D.

There are few references reporting numerical solutions to the Cahn–Hilliard phase-field model with degenerate mobility and logarithmic free energy. To our knowledge, the numerical solutions presented in the literature are limited to the early part of the simulation in 2D domains. We present herein stationary solutions in 3D domains.

4.2.1. $\alpha = 200$ and $\bar{c} = 0.63$

We computed the solution on a 128^3 mesh. We plot the evolution of the statistical moments of order 2, 4 (Fig. 24) and 3 (Fig. 25). The evolution of the Ginzburg–Landau free energy is depicted in Fig. 26. We present snapshots of isosurfaces of the concentration in Fig. 27. We observe that the randomly perturbed constant concentration evolves to a complex interconnected pattern. We did not find any sign of nucleation for this example, in contrast with the 2D counterpart of this problem (see Section 4.1.1). The steady state solution is a cylinder, which is one of the conjectured solutions for the periodic isoperimetric problem.

4.2.2. $\alpha = 600$ and $\bar{c} = 0.75$

In the 2D case there are small topological differences between $\bar{c} = 0.63$ and $\bar{c} = 0.75$, but in the 3D problem there are significant differences. In the latter case, we found that one of the species nucleated. As before, the steady state is a cylinder.

We computed the solution on a 128^3 mesh. We plot the evolution of the statistical moments of order 2, 4 (Fig. 28) and 3 (Fig. 29). The evolution of the Ginzburg–Landau free energy is depicted in Fig. 30. We present snapshots of isosurfaces of the concentration in Fig. 31.

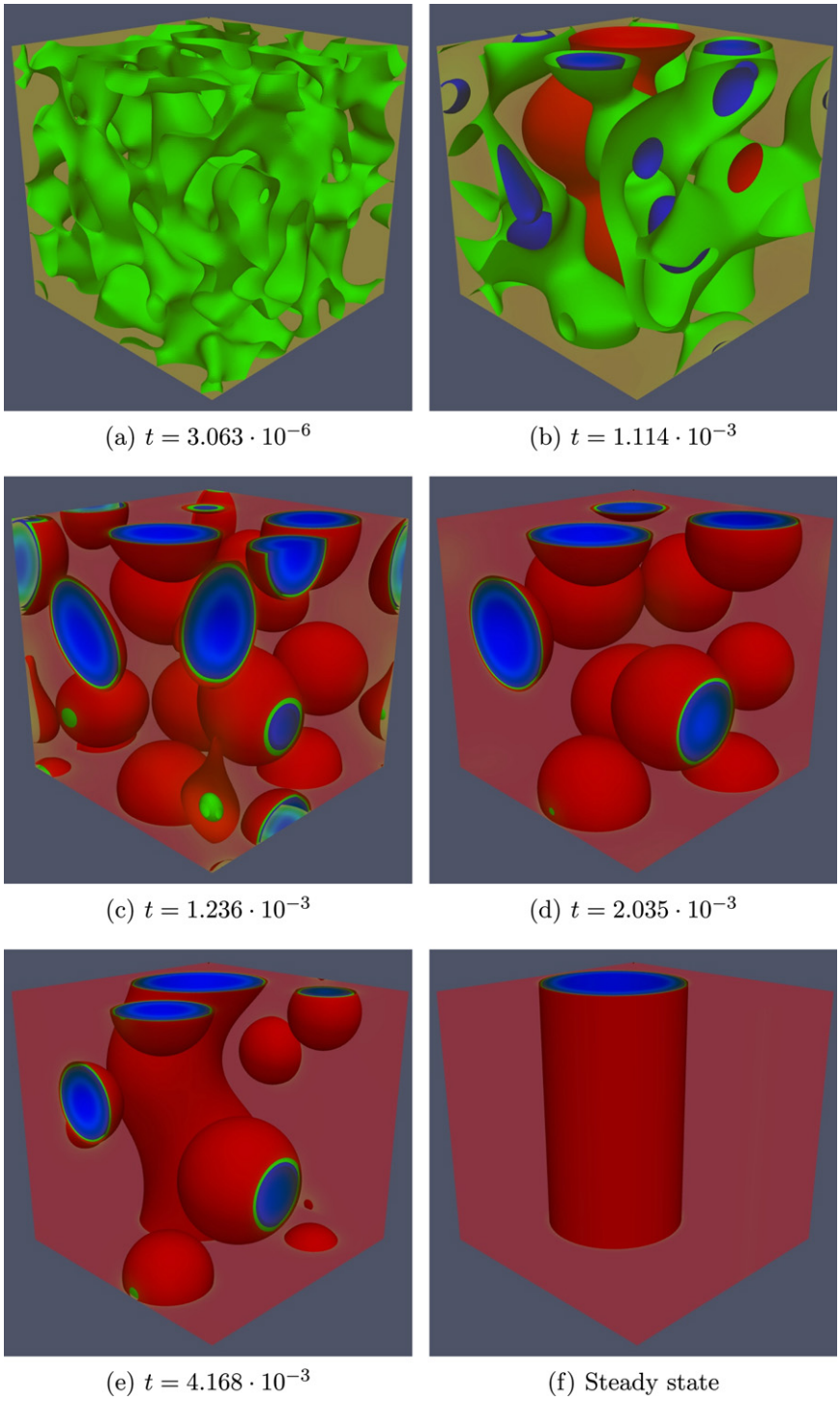

Fig. 31. Evolution of the concentration from a randomly perturbed initial condition for $\alpha = 600$ and $\bar{c} = 0.75$. The mesh is comprised of 128^3 quadratic elements.

5. Conclusions

We presented a numerical methodology for the approximation of the general Cahn–Hilliard phase-field model. Our method is based on isogeometric analysis, which allows us to generate the $\mathscr{C}^1$-continuous functions required to solve the Cahn–Hilliard equation in a primal variational framework.

We introduced an adaptive time-stepping algorithm which proved to be very effective for this highly nonlinear problem. We were able to compute steady state solutions in two and three dimensions. The spatial resolution has a significant effect on the numerical solution at the steady state. Non-physical solutions are obtained at the steady state when the spatial mesh is not fine enough, a shortcoming not previously emphasized in the literature. However, this effect is not observed in the early dynamics of the problem.

In the future we envision combining NURBS discretizations that are at least $\mathscr{C}^1$-continuous at patch level and employing the CDG approach of [29,76] at the patch boundaries. We feel that this would provide a good compromise between geometrical flexibility

and computational efficiency. We note, however, that progress in computational geometry suggests that $\mathscr{C}^1$-continuous basis, at least defined almost everywhere, may be a real possibility in the near future.

The computations we performed demonstrated that our method is capable of giving very accurate and stable results even when the solution possesses very thin layers that evolve and propagate over the mesh. From the numerical analysis point of view, it seems apparent that the length-scale parameter associated with the thickness of interfaces should be redefined in terms of the resolution of the mesh. Studies adopting this approach resulted in solution topology insensitive to mesh refinement even for very coarse discretizations, whereas employing a fixed length-scale parameter led to unphysical solutions on coarse meshes. Further studies of a theoretical nature investigating this point should prove highly valuable. Nevertheless, this observation has already illustrated the potential of elevating phase-field modeling from the realm of purely scientific interest to a practical engineering level.

There is also room for improvement in the Cahn–Hilliard model. We found that in the case of nucleation the coarsening process does not take place only through bubbles merging. Some of them vanish without any contact with other bubbles. Conservation of the formulation creates a non-local "worm hole" effect in which distant bubbles enlarge when other non-contiguous bubbles vanish. We observed this behavior even for fairly large values of the thickness parameter ($\alpha \approx 25,000$).

In summary, this paper constitutes a first step in the application of isogeometric analysis to phase-fields models. Although our initial efforts were focused on the Cahn–Hilliard equation, we feel that the methodology presented herein shows the way to applications to other areas of engineering interest involving higher-order spatial operators, such as, for example, liquid–vapor flows, rotation-free thin shell theory, strain-gradient elastic and inelastic material models, and dynamic crack propagation.

Acknowledgements

H. Gómez gratefully acknowledges the support provided by *Ministerio de Educación y Ciencia* through the postdoctoral fellowships program. Funding provided by *Xunta de Galicia* (Grants No. PGIDIT05PXIC118002PN and No. PGDIT06TAM11801PR), *Ministerio de Educación y Ciencia* (Grants No. DPI2004-05156, # DPI2006-15275 and # DPI2007-61214) cofinanced with FEDER funds, *Universidad de A Coruña* and *Fundación de la Ingeniería Civil de Galicia* is also acknowledged by H. Gómez. Y. Bazilevs was partially supported by the J.T. Oden ICES Postdoctoral Fellowship at the Institute for Computational Engineering and Sciences. V.M. Calo, Y. Bazilevs and T.J.R Hughes were partially supported by the Office of Naval Research under Contract No. N00014-03-0263 and under the MURI program (18412450-35520-B).

References

[1] H. Abels, M. Wilke, Convergence to equilibrium for the Cahn–Hilliard equation with a logarithmic free energy, Nonlinear Anal.: Theory Methods Appl. 67 (2007) 3176–3193.
[2] D.M. Anderson, G.B. McFadden, A.A. Wheeler, Diffuse-interface methods in fluid mechanics, Annu. Rev. Fluid Mech. 30 (1998) 139–165.
[3] I. Akkerman, Y. Bazilevs, V.M. Calo, T.J.R. Hughes, S. Hulshoff, The role of continuity in residual-based variational multiscale modeling of turbulence, Comput. Mech. 41 (2007) 371–378.
[4] J.W. Barret, J.F. Blowey, H. Garcke, Finite element approximation of the Cahn–Hilliard equation with degenerate mobility, SIAM J. Numer. Anal. 37 (1999) 286–318.
[5] J.W. Barrett, H. Garcke, R. Nurnberg, Finite element approximation of a phase field model for surface diffusion of voids in a stressed solid, Math. Comput. 75 (2006) 7–41.
[6] G.K. Batchelor, An Introduction to Fluid Dynamics, Cambridge University Press, 1967.
[7] Y. Bazilevs, V.M. Calo, J.A. Cottrell, T.J.R. Hughes, A. Reali, G. Scovazzi, Variational multiscale residual-based turbulence modeling for large eddy simulation of incompressible flows, Comput. Methods Appl. Mech. Engrg. 197 (2007) 173–201.
[8] G. Benderskaya, M. Clemens, H. De Gersem, T. Weiland, Embedded Runge–Kutta methods for field-circuit coupled problems with switching elements, IEEE Trans. Magn. 41 (2005) 1612–1615.
[9] J.F. Blowey, C.M. Elliott, The Cahn–Hilliard gradient theory for phase separation with non-smooth free energy. Part II: numerical analysis, Eur. J. Appl. Math. 3 (1992) 147–149.
[10] G. Caginalp, Stefan and Hele–Shaw type models as asymptotic limits of the phase field equations, Phys. Rev. A 39 (1989) 5887–5896.
[11] J.W. Cahn, On spinodal decomposition, Acta Metall. 9 (1961) 795–801.
[12] J.W. Cahn, J.E. Hilliard, Free energy of a non-uniform system. I. Interfacial free energy, J. Chem. Phys. 28 (1958) 258–267.
[13] J.W. Cahn, J.E. Hilliard, Free energy of a non-uniform system. III. Nucleation in a two-component incompressible fluid, J. Chem. Phys. 31 (1959) 688–699.
[14] H.D. Ceniceros, A.M. Roma, A nonstiff adaptive mesh refinement-based method for the Cahn–Hilliard equation, J. Comput. Phys. 225 (2007) 1849–1862.
[15] R. Chella, J. Viñals, Mixing of a two-phase fluid by cavity flow, Phys. Rev. E 53 (1996) 3832–3840.
[16] L.Q. Chen, Phase-field models for microstructural evolution, Annu. Rev. Mater. Res. 32 (2002) 113–140.
[17] R. Choksi, P. Sternberg, Periodic phase separation: the periodic Cahn–Hilliard and the isoperimetric problems, Interfaces Free Bound. 8 (2006) 371–392.
[18] J. Chung, G.M. Hulbert, A time integration algorithm for structural dynamics with improved numerical dissipation: The generalized-α method, J. Appl. Mech. 60 (1993) 371–375.
[19] M.I.M. Copetti, C.M. Elliott, Numerical analysis of the Cahn–Hilliard equation with a logarithmic free energy, Numer. Math. 63 (1992) 39–65.
[20] J.A. Cottrell, T.J.R. Hughes, A. Reali, Studies of refinement and continuity in isogeometric structural analysis, Comput. Methods Appl. Mech. Engrg. 196 (2007) 4160–4183.
[21] J. Crank, Free and Moving Boundary Problems, Oxford University Press, 1997.
[22] A. Debussche, L. Dettori, On the Cahn–Hilliard equation with a logarithmic free energy, Nonlinear Anal. 24 (1995) 1491–1514.
[23] I.C. Dolcetta, S.F. Vita, R. March, Area preserving curve-shortening flows: from phase separation to image processing, Interfaces Free Bound. 4 (2002) 325–343.
[24] Q. Du, R.A. Nicolaides, Numerical analysis of a continuum model of phase transition, SIAM J. Numer. Anal. 28 (1991) 1310–1322.
[25] C.M. Elliott, D.A. French, Numerical studies of the Cahn–Hilliard equation for phase separation, IMA J. Appl. Math. 38 (1987) 97–128.
[26] C.M. Elliott, D.A. French, F.A. Milner, A 2nd-order splitting method for the Cahn–Hilliard equation, Numer. Math. 54 (1989) 575–590.
[27] C.M. Elliott, H. Garcke, On the Cahn–Hilliard equation with degenerate mobility, SIAM J. Math. Anal. 27 (1996) 404–423.
[28] C.M. Elliott, S. Zheng, On the Cahn–Hilliard equation, Arch. Ration. Mech. Anal. 96 (1986) 339–357.
[29] G. Engel, K. Garikipati, T.J.R. Hughes, M.G. Larson, L. Mazzei, R.L. Taylor, Continuous/discontinuous finite element approximations of fourth-order elliptic problems in structural and continuum mechanics with applications to thin beams and plates, and strain gradient elasticity, Comput. Methods Appl. Mech. Engrg. 191 (2002) 3669–3750.
[30] D.N. Fan, L.Q. Chen, Diffuse interface description of grain boundary motion, Philos. Mag. Lett. 75 (1997) 187–196.
[31] X. Feng, A. Prohl, Analysis of a fully discrete finite element method for phase field model and approximation of its sharp interface limits, Math. Comput. 73 (2003) 541–547.
[32] I. Fonseca, M. Morini, Surfactants in foam stability: a phase field model, Arch. Ration. Mech. 183 (2007) 411–456.
[33] H.B. Frieboes, J.P. Sinek, S. Sanga, F. Gentile, A. Granaldi, P. Decuzzi, C. Cosentino, F. Amato, M. Ferrari, V. Cristini, Towards multiscale modeling of nanovectored delivery of therapeutics to cancerous lesions, Biomed. Dev. in press.
[34] E. Fried, M.E. Gurtin, Dynamic solid–solid transitions with phase characterized by an order parameter, Physica D 72 (1994) 287–308.
[35] D. Furihata, A stable and conservative finite difference scheme for the Cahn–Hilliard equation, Numer. Math. 87 (2001) 675–699.
[36] H. Garcke, B. Nestler, A mathematical model for grain growth in thin metallic films, Math. Models Methods Appl. Sci. 10 (2000) 895–921.
[37] H. Garcke, B. Nestler, B. Stinner, A diffuse interface model for alloys with multiple components and phases, SIAM J. Appl. Math. 64 (2004) 775–799.
[38] H. Garcke, B. Nestler, B. Stoth, On anisotropic order parameter models for multiphase systems and their sharp interface limits, Physica D 115 (1998) 87–108.
[39] H. Garcke, B. Niethammer, M. Rumpf, U. Weikard, Transient coarsening behaviour in the Cahn–Hilliard model, Acta Mater. 51 (2003) 2823–2830.
[40] H. Garcke, A. Novick-Cohen, A singular limit for a system of degenerate Cahn–Hilliard equations, Adv. Differ. Eq. 5 (2000) 401–434.
[41] K. Gustafsson, Control-theoretic techniques for stepsize selection in implicit Runge–Kutta methods, ACM Trans. Math. Software 20 (1994) 496–517.
[42] L. Hauswirth, J. Pérez, P. Romon, A. Ros, The periodic isoperimetric problem, Trans. AMS 356 (2004) 2025–2047.
[43] Y. He, Y. Liu, T. Tang, On large time-stepping methods for the Cahn–Hilliard equation, Appl. Numer. Math. 57 (2007) 616–628.

[44] T.J.R. Hughes, Multiscale phenomena: Green's functions, the Dirichlet-to-Neumann formulation, subgrid-scale models, bubbles and the origin of stabilized methods, Comput. Methods Appl. Mech. Engrg. 127 (1995) 387–401.
[45] T.J.R. Hughes, The Finite Element Method: Linear Static and Dynamic Finite Element Analysis, Dover Publications, Mineola, NY, 2000.
[46] T.J.R. Hughes, J.A. Cottrell, Y. Bazilevs, Isogeometric analysis: CAD, finite elements, NURBS, exact geometry and mesh refinement, Comput. Methods Appl. Mech. Engrg. 194 (2005) 4135–4195.
[47] T.J.R. Hughes, G.R. Feijóo, L. Mazzei, J.-B. Quincy, The Variational Multiscale Method — a paradigm for computational mechanics, Comput. Methods Appl. Mech. Engrg. 166 (1998) 3–24.
[48] K.E. Jansen, C.H. Whiting, G.M. Hulbert, A generalized-α method for integrating the filtered Navier–Stokes equations with a stabilized finite element method, Comput. Methods Appl. Mech. Engrg. 190 (1999) 305–319.
[49] J.-H. Jeong, N. Goldenfeld, J.A. Dantzig, Phase field model for three-dimensional dendritic growth with fluid flow, Phys. Rev. E 64 (2001) 1–14.
[50] Y. Jingxue, L. Changchun, Regularity of solutions of the Cahn–Hilliard equation with concentration dependent mobility, Nonlinear Anal. 45 (2001) 543–554.
[51] D. Kay, R. Welford, A multigrid finite element solver for the Cahn–Hilliard equation, J. Comput. Phys. 212 (2006) 288–304.
[52] J. Kim, K. Kang, J. Lowengrub, Conservative multigrid methods for Cahn–Hilliard fluids, J. Comput. Phys. 193 (2004) 511–543.
[53] Y.-T. Kim, N. Provatas, N. Goldenfeld, J.A. Dantzig, Universal dynamics of phase field models for dendritic growth, Phys. Rev. E 59 (1999) 2546–2549.
[54] D.E. Knuth, The Art of Computing Programming, vol. 2, Addison-Wesley, 1997.
[55] D.J. Korteweg, Sur la forme que prenent les équations du mouvements des fluides si l'on tient compte des forces capilaires causées par des variations de densité considérables mains continues et sur la théorie de la capillarité dans l'hypothése d'une varation continue de la densité, Arch. Néerl Sci. Exactes Nat. Ser. II 6 (1901) 124.
[56] L.D. Landau, V.I. Ginzburg, On the theory of superconductivity, in: L.D. Landau, D. ter Haar (Eds.), Collected Papers, Pergamon Oxford, 1965, pp. 626–633.
[57] J. Lang, Two-dimensional fully adaptive solutions of reaction-diffusion equations, Appl. Numer. Math. 18 (1995) 223–240.
[58] H.-G. Lee, J.S. Lowengrub, J. Goodman, Modeling pinchoff and reconnection in a Hele–Shaw cell. II. Analysis and simulation in the nonlinear regime, Phys. Fluids 14 (2002) 514–545.
[59] J. Lighthill, Waves in Fluids, Cambridge University Press, 1978.
[60] C. Liu, J. Shen, A phase field model for the mixture of two incompressible fluids and its approximation by a Fourier-spectral method, Physica D 179 (2003) 211–228.
[61] J. Lowengrub, L. Truskinovsky, Quasi-incompressible Cahn–Hilliard fluids and topological transitions, Proc. Roy. Soc. London Ser. A 454 (1998) 2617–2654.
[62] L. Modica, The gradient theory of phase transitions and the minimal interface criterion, Arch. Ration. Mech. Anal. 98 (1987) 123–142.
[63] W. Ostwald, Lehrbruck der Allgemeinen Chemie (2) (1896).
[64] O. Penrose, P.C. Fife, Thermodynamically consistent models of phase field type for the kinetics of phase transition, Physica D 43 (1990) 44–62.
[65] Y. Saad, M.H. Schultz, GMRES: a generalized minimal residual algorithm for solving nonsymmetric linear systems, SIAM J. Sci. Stat. Comput. 7 (1986) 856–869.
[66] T.N. Sederberg, J.M. Zheng, A. Bakenov, A. Nasri, T-Splines and T-NURCCSs, ACM Trans. Graphics 22 (2003) 477–484.
[67] P. Sternberg, The effect of singular perturbation on nonconvex variational problems, Arch. Ration. Mech. Anal. 101 (1988) 209–260.
[68] R.H. Stogner, G.F. Carey, C^1 macroelements in adaptive finite element methods, Int. J. Numer. Methods Engrg. 70 (2007) 1076–1095.
[69] Z.Z. Sun, A second order accurate linearized difference scheme for the two-dimensional Cahn–Hilliard equation, Math. Comput. 64 (1995) 1463–1471.
[70] R. Toral, A. Chakrabarti, J.D. Gunton, Large scale simulations of the two-dimensional Cahn–Hilliard model, Physica A 213 (1995) 41–49.
[71] S. Tremaine, On the origin of irregular structure in Saturn's rings, Astron. J. 125 (2003) 894–901.
[72] H.S. Udaykumar, R. Mittal, W. Shyy, Computation of solid–liquid phase fronts in the sharp interface limit on fixed grids, J. Comput. Phys. 153 (1999) 535–574.
[73] P.J. van der Houwen, B.P. Sommeijer, W. Couzy, Embedded diagonally implicit Runge–Kutta algorithms on parallel computers, Math. Comput. 58 (1992) 135–159.
[74] J.D. van der Waals, The thermodynamics theory of capillarity under the hypothesis of a continuous variation of density, J. Stat. Phys. 20 (1979) 197–244.
[75] B.P. Vollmayr-Lee, A.D. Rutemberg, Fast and accurate coarsening simulation with an unconditionally stable time step, Phys. Rev. E 68 (2003) 066703.
[76] G.N. Wells, E. Kuhl, K. Garikipati, A discontinuous Galerkin method for the Cahn–Hilliard equation, J. Comput. Phys. 218 (2006) 860–877.
[77] Y. Xia, Y. Xu, C.-W. Shu, Local discontinuous Galerkin methods for the Cahn–Hilliard type equations, J. Comput. Phys. 227 (2007) 472–491.
[78] X. Ye, X. Cheng, The Fourier spectral method for the Cahn–Hilliard equation, Appl. Math. Comput. 171 (2005) 345–357.
[79] J. Zhu, L.-Q. Chen, J. Shen, V. Tikare, Coarsening kinetics from a variable-mobility Cahn–Hilliard equation: application of a semi-implicit Fourier-spectral method, Phys. Rev. E 60, 3564–3572.